ATLAS CONF Note

ATLAS-CONF-2021-022

14th June 2021

Search for charginos and neutralinos in final states with two boosted hadronically decaying bosons and missing transverse momentum in pp collisions at $\sqrt{s} = 13$ TeV with the ATLAS detector

The ATLAS Collaboration

A search for charginos and neutralinos at the Large Hadron Collider is reported using fully hadronic final states and missing transverse momentum. Pair-produced charginos or neutralinos are explored, each decaying into a high-p_{T} Standard Model weak boson. Fully-hadronic final states are studied to exploit the advantage of the large branching ratio, and the efficient background rejection by identifying the high-p_{T} bosons using large-radius jets and jet substructure information. An integrated luminosity of 139 fb^{-1} of proton-proton collision data collected by the ATLAS detector at a center-of-mass energy of 13 TeV is used. No significant excess is found beyond the Standard Model expectation. The 95% confidence level exclusion limits are set on wino or higgsino production with varying assumptions in the decay branching ratios and the type of the lightest supersymmetric particle. A wino (higgsino) mass up to 1060 (900) GeV is excluded when the lightest SUSY particle mass is below 400 (240) GeV.

ATLAS-CONF-2021-022
14 June 2021

1 Introduction

Supersymmetry (SUSY) [1–6] is a theoretical framework that extends the Standard Model (SM) by introducing new particles ("superpartners") that have identical quantum numbers with the SM particles except for their spins. In the Minimal Supersymmetric Standard Model (MSSM), bino ($\widetilde{B}$), wino ($\widetilde{W}$) and higgsino ($\widetilde{H}$) are the superpartners of the $U(1)_Y$ and $SU(2)$ gauge fields and the Higgs field, respectively. These are collectively referred to as "electroweakinos" and form the chargino ($\widetilde{\chi}_1^{\pm}, \widetilde{\chi}_2^{\pm}$) and neutralino ($\widetilde{\chi}_1^0, \widetilde{\chi}_2^0, \widetilde{\chi}_3^0, \widetilde{\chi}_4^0$) mass eigenstates through a mixing, with the subscripts indicating increasing mass. The lightest neutralino ($\widetilde{\chi}_1^0$) is often considered to be the lightest SUSY particle (LSP), since it is then a viable candidate of weakly interacting massive particle dark matter [7, 8] when R-parity conservation is assumed [9]. Depending on the signal model, the superpartner of the graviton (gravitino; $\widetilde{G}$) and the axion (axino; $\tilde{a}$) are also considered to be the LSP and dark matter candidate in this search.

Electroweakinos with $O(100$ GeV$)$ – $O(1$ TeV$)$ masses are motivated by various phenomenological arguments: (1) the mass of the neutralino LSP dark matter is constrained to be less than a few TeV by the observed relic density [10, 11]; (2) the higgsino mass is also motivated to be of the same order as the Z-boson mass by naturalness arguments [12–15]; (3) the MSSM parameter space consistent with the potential muon g-2 anomaly tends to include electroweakinos with masses from 200 GeV to 1 TeV [16, 17].

This search targets the pair production of electroweakinos ($\widetilde{\chi}_{\text{heavy}}$), where each of them decays into a lighter one ($\widetilde{\chi}_{\text{light}}$) and an on-shell W, Z or the SM-like Higgs boson (h). The search presented here assumes that the mass splitting $\Delta m(\widetilde{\chi}_{\text{heavy}}, \widetilde{\chi}_{\text{light}})$ is greater than 400 GeV. $\widetilde{\chi}_{\text{heavy}}$ can be either wino- or higgsino-like, and $\widetilde{\chi}_{\text{light}}$ can be a bino-, wino-, higgsino-like chargino/neutralino, gravitino or axino as discussed more in Section 2. Cases where both $\widetilde{\chi}_{\text{heavy}}$ and $\widetilde{\chi}_{\text{light}}$ are wino- or higgsino-like are not considered. $\widetilde{\chi}_{\text{light}}$ is either the LSP or an electroweakino nearly degenerate with it, creating missing transverse momentum ($\mathbf{p}_{\text{T}}^{\text{miss}}$, with the magnitude $E_{\text{T}}^{\text{miss}}$) in the signature. [1]

The analysis focuses on the hadronic decay modes of the W, Z and h bosons, namely $W \to q\bar{q}$, $Z \to q\bar{q}/b\bar{b}$ and $h \to b\bar{b}$ where q ($\bar{q}$) represents light-flavor (anti-)quarks u, d, s, c ($\bar{u}, \bar{d}, \bar{s}, \bar{c}$).[2] Two fully-hadronic final states are considered; the $qqqq$ final state which involves two W/Z bosons decaying into two light-flavor (anti-)quarks; and the $bbqq$ final state where a W/Z boson decays into two light-flavor (anti-)quarks and a Z/h boson decays into $b\bar{b}$, as illustrated by the diagrams in Figure 1. Final states with four b-quarks are not considered in this search. [3] While the ATLAS and CMS experiments have typically searched for the pair-production of electroweakinos using leptonic decay modes [18–33], the fully-hadronic final states take advantage of the larger W, Z, and h hadronic branching ratios, and thereby provide sensitivity to the production of heavier electroweakinos, despite their smaller production cross-sections.

The multi-jet background is highly suppressed by the large $E_{\text{T}}^{\text{miss}}$ requirement, and the dominant backgrounds in the analysis are $Z(\to \nu\nu)$ + jets, $W(\to \ell\nu)$ + jets, and di-boson production. These can be effectively suppressed when targeting large mass splittings between the produced electroweakinos and the LSP, by selecting high-p_{T} kinematics and explicitly reconstructing the two boosted SM bosons. The "boson tagging"

[1] Note that in the regime of large mass splitting, the effect of chargino/neutralino mixing is highly suppressed so that the gauge eigenstates (e.g. bino) and the mass eigenstates (e.g. bino-like $\widetilde{\chi}_1^0$) can be regarded as almost identical. Therefore in this paper we do not make the distinction and "electroweakinos" are defined to represent both unless explicitly stated otherwise.

[2] Note that in this paper the symbol q (b) represents both quarks and anti-quarks unless mentioned explicitly since they are not distinguished in the search. Note also that charm (anti-)quarks are treated as light-flavor (anti-)quarks in the analysis.

[3] The contribution from signals with two h-bosons are included in the signal models although not targeted. Likewise, all the decays of W, Z and h are taken into account for the signals.

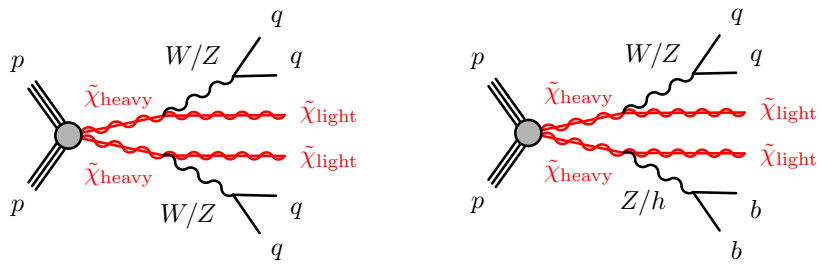

(a) $qqqq$ final state (b) $bbqq$ final state

Figure 1: Diagram for the targeted signatures and final states.

technique developed by ATLAS and CMS experiments [34–37] is employed, where a single large-radius jet is used to capture the two collimated energetic jets from each SM boson decay. Analysis of the substructure helps to identify the hadronic decays of W, Z, and h. The introduction of this technique significantly improves the previous fully-hadronic final state analysis in ATLAS targeting the $bbqq$ final state [22], and establishes the sensitivity of the $qqqq$ final state for the first time at the Large Hadron Collider (LHC), achieving the unprecedented search sensitivity to electroweakinos as heavy as 1 TeV.

This search uses proton-proton collision data collected by the ATLAS detector in the years 2015–2018 at a center-of-mass energy of $\sqrt{s} = 13$ TeV, corresponding to an integrated luminosity of 139 fb^{-1}. The results are interpreted in terms of various models with different electroweakino types for ($\widetilde{\chi}_{\text{heavy}}$, $\widetilde{\chi}_{\text{light}}$) and their branching ratio assumptions. While each model predicts different electroweakino branching ratios into W, Z or h, the search combines the dedicated event selections for each decay to achieve a small model dependency.

2 Target physics scenarios and the signal models

Three physics scenarios are considered in the analysis:

- a baseline MSSM scenario where bino, wino and higgsino are considered as $\widetilde{\chi}_{\text{heavy}}$ or $\widetilde{\chi}_{\text{light}}$;
- a scenario with gravitino LSP and light higgsinos inspired by the general gauge mediation (GGM) models and naturalness;
- and a scenario with axino LSP assuming the SM extension with a QCD axion and light higgsinos driven by naturalness.

The signal models considered in the analysis, derived by each physics scenario, are described in the following sub-sections. Each model is labeled as (A, B), where A and B represent the dominant component of $\widetilde{\chi}_{\text{heavy}}$ and $\widetilde{\chi}_{\text{light}}$ respectively. All the SUSY particles other than $\widetilde{\chi}_{\text{heavy}}$ and $\widetilde{\chi}_{\text{light}}$ are assumed to be decoupled in mass [38, 39]. The production modes, final states, and the branching ratio assumptions for $\widetilde{\chi}_{\text{heavy}}$ are summarized in Table 1.

The wino-like states form a doublet consisting of one chargino and one neutralino, while the higgsino-like triplet includes an additional neutralino. The mass degeneracy within these wino/higgsino multiplets is dictated by the extent of mixing with the other electroweakino states, which is characterized by $\Delta m(\widetilde{\chi}_{\text{heavy}}, \widetilde{\chi}_{\text{light}})$. With $\Delta m(\widetilde{\chi}_{\text{heavy}}, \widetilde{\chi}_{\text{light}}) > 400$ GeV, the mass splittings within the wino/higgsino

multiplets are typically small (< 10 GeV), such that the decay products are almost never reconstructed in this analysis. Therefore, these multiplets are treated as approximately degenerate; the masses of wino-like chargino and wino-like neutralino are treated as identical; and the masses of higgino-like chargino and the heavier higgsino-like neutralino are set 1 GeV heavier than the lighter higgsino-like neutralino.[4] Particles originating from decays within the wino doublet or higgsino triplet are ignored so that only the decays of the form $\widetilde{\chi}_{\text{heavy}} \to \widetilde{\chi}_{\text{light}} + W/Z/h$ are taken into account in the signature.

2.1 Bino/wino/higgsino LSP models: $(\widetilde{W}, \widetilde{B})$, $(\widetilde{W}, \widetilde{H})$, $(\widetilde{H}, \widetilde{B})$, $(\widetilde{H}, \widetilde{W})$

Two of $\widetilde{B}$, $\widetilde{W}$, and $\widetilde{H}$ are assumed to be light enough to be produced at the LHC while the others are decoupled. Four mass hierarchies are experimentally explorable under the regime: $(\widetilde{W}, \widetilde{B})$, $(\widetilde{W}, \widetilde{H})$, $(\widetilde{H}, \widetilde{B})$, $(\widetilde{H}, \widetilde{W})$. Bino is not considered as $\widetilde{\chi}_{\text{heavy}}$ here since the production cross-section is negligible when sfermions and the non-SM Higgs bosons are decoupled. The mass spectra, corresponding mass eigenstates, and the decays considered are illustrated for each case in Figure 2. A W-boson is generated when a chargino decays into a neutralino or vice versa; a Z- or h-boson is emitted when a chargino decays into a chargino, or a neutralino decays into a neutralino.

The production modes considered in each model are shown in Table 1. Processes involving chargino-chargino and chargino-neutralino pair production are taken into account in the wino production models: $(\widetilde{W}, \widetilde{B})$ and $(\widetilde{W}, \widetilde{H})$; and neutralino-neutralino production is additionally included for the higgsino production models: $(\widetilde{H}, \widetilde{B})$ and $(\widetilde{H}, \widetilde{W})$.[5]

The branching ratios of $\widetilde{\chi}_{\text{heavy}}$ are treated as follows. In the $(\widetilde{W}, \widetilde{B})$ and $(\widetilde{H}, \widetilde{B})$ models, the produced chargino ($\widetilde{\chi}_1^{\pm}$) decays with 100% probability into the bino LSP ($\widetilde{\chi}_1^0$) and a W-boson. Meanwhile, the produced neutralino(s) can decay either into Z or into h.[6] Given the complicated model dependency, the branching ratio of the second lightest neutralino ($\widetilde{\chi}_2^0$) is treated as a free parameter,[7] and $\mathcal{B}(\widetilde{\chi}_2^0 \to Z\widetilde{\chi}_1^0)(= 1 - \mathcal{B}(\widetilde{\chi}_2^0 \to h\widetilde{\chi}_1^0))$ is scanned over 0%, 25%, 50%, 75% and 100% in both models. For the $(\widetilde{H}, \widetilde{B})$ model, the branching ratios of the heavy neutral higgsino ($\widetilde{\chi}_3^0$) are fixed with respect to those of the light neutral higgsino ($\widetilde{\chi}_2^0$) via:

- $\mathcal{B}(\widetilde{\chi}_2^0 \to Z\widetilde{\chi}_1^0) + \mathcal{B}(\widetilde{\chi}_3^0 \to Z\widetilde{\chi}_1^0) = 1$,
- $\mathcal{B}(\widetilde{\chi}_2^0 \to h\widetilde{\chi}_1^0) + \mathcal{B}(\widetilde{\chi}_3^0 \to h\widetilde{\chi}_1^0) = 1$.

These provide a good approximation when $\Delta m(\widetilde{\chi}_{\text{heavy}}, \widetilde{\chi}_{\text{light}})$ is significantly larger than m_h [40].

In $(\widetilde{W}, \widetilde{H})$ and $(\widetilde{H}, \widetilde{W})$ models, however, the branching ratios of the produced chargino and neutralino(s) are largely dictated by the three MSSM parameters; the wino mass parameter M_2, the higgsino mass parameter μ, and the ratio of vacuum expectation values of the two Higgs fields $\tan\beta$. For a given set of $(M_2, \mu, \tan\beta)$ the branching ratios are coherently derived using SOFTSUSY 4.1.7 [41, 42], with all the SUSY mass parameters except for M_2 and μ are set as decoupled The signal models are tested using various

[4] The 1 GeV mass splitting is used to avoid potential technical issues when setting exactly zero. This choice is arbitrary and has no impact on the analysis.

[5] Neutral wino pairs can only be produced via a t-channel exchanging squarks, which is prohibited when squarks are assumed to be decoupled.

[6] Produced heavier higgsinos are assumed to decay 100% directly into bino rather than the lighter higgsino, which is reasonable given the much smaller higgsino mass splitting compared with the higgsino-bino mass splitting.

[7] Particularly for $(\widetilde{W}, \widetilde{B})$, the branching ratio strongly depends on the higgsino mass as the decay has to rely on the small higgsino component, even though it is assumed to be decoupled.

combinations of $(M_2, \mu, \tan\beta)$ where $M_2 \in [0, 1.2]$ TeV, $\mu \in [-1.2, 1.2]$ TeV, and $\tan\beta = 2, 5, 10, 30$ are considered.

The vast majority of the previous eletroweakino searches at the LHC have targeted the simplified $(\widetilde{W}, \widetilde{B})$ model, where only a specific production channel and decay mode are considered (detailed in Section 4.2.2). For $\widetilde{\chi}_1^{\pm}\widetilde{\chi}_1^{\mp}$ production with decays into WW, $m(\widetilde{\chi}_1^{\pm}) < 400$ GeV is excluded for $m(\widetilde{\chi}_1^0) < 200$ GeV [18, 27]. For $\widetilde{\chi}_1^{\pm}\widetilde{\chi}_2^0$ production, $m(\widetilde{\chi}_1^{\pm}/\widetilde{\chi}_2^0) < 640$ GeV is excluded for $m(\widetilde{\chi}_1^0) < 300$ GeV when the $\widetilde{\chi}_2^0$ is assumed to decay into Z and $\widetilde{\chi}_1^0$ with 100% probability [19–21, 28, 29]. Alternatively, $m(\widetilde{\chi}_1^{\pm}/\widetilde{\chi}_2^0) < 740$ GeV is excluded for $m(\widetilde{\chi}_1^0) < 250$ GeV [22–24, 30–32] when the $\widetilde{\chi}_2^0$ decays solely into h and $\widetilde{\chi}_1^0$.

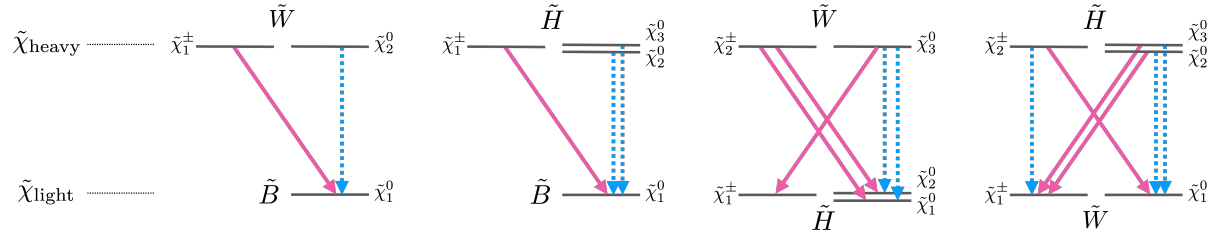

(a) $(\tilde{W}, \tilde{B})$ (b) $(\tilde{H}, \tilde{B})$ (c) $(\tilde{W}, \tilde{H})$ (d) $(\tilde{H}, \tilde{W})$

Figure 2: The electroweakino mass spectra and corresponding mass eigenstates in each mass hierarchy in each model in the bino/wino/higgsino LSP scenario. The solid (dashed) arrows represent the decay modes emitting a W (Z or h). A W-boson is generated when a chargino decays into a neutralino or vice versa; and a Z- or h-boson is emitted when a chargino decays into a chargino or a neutralino decays into a neutralino.

2.2 GGM/Naturalness-driven gravitino LSP model: $(\widetilde{H}, \widetilde{G})$

General gauge mediation (GGM) [43–47], a class of SUSY breaking scenarios characterized by a messenger sector to which only SM gauge bosons can couple, typically predicts a nearly massless Gravitino $(\widetilde{G})$ as the LSP. Motivated also by the naturalness argument, the production of a relatively light higgsino triplet $(\widetilde{\chi}_1^{\pm}, \widetilde{\chi}_2^0, \widetilde{\chi}_1^0)$ decaying into a gravitino LSP has been explored at ATLAS [25, 26] and CMS [29], as illustrated in Figure 3(a). All of the four production modes are considered together: $\widetilde{\chi}_1^{\pm}\widetilde{\chi}_1^{\mp}$, $\widetilde{\chi}_1^{\pm}\widetilde{\chi}_1^0$, $\widetilde{\chi}_1^{\pm}\widetilde{\chi}_2^0$, $\widetilde{\chi}_1^0\widetilde{\chi}_2^0$. A moderately small higgsino-gravitino coupling is considered in this analysis where the produced heavy higgsinos $(\widetilde{\chi}_1^{\pm}/\widetilde{\chi}_2^0)$ always decay into a gravitino via the lightest neutral higgsino $(\widetilde{\chi}_1^0)$, while the $\widetilde{\chi}_1^0$ still has short enough life-time to be regarded as a prompt decay. In this model, the $\widetilde{\chi}_1^0$ decays into a gravitino and either a Z- or h-boson, where the branching ratio $\mathcal{B}(\widetilde{\chi}_1^0 \to Z\widetilde{G})(= 1 - \mathcal{B}(\widetilde{\chi}_1^0 \to h\widetilde{G}))$ is treated as a free parameter and scanned in the limit setting. The previous searches have excluded mass of $\widetilde{\chi}_1^0$ lighter than 650–880 GeV depending on the branching ratio [25, 26, 29].

2.3 Naturalness-driven axino LSP model: $(\widetilde{H}, \tilde{a})$

While the QCD Lagrangian generally allows for CP violation, the absence of such an observation suggests a highly unnatural tuning of the parameters in the theory, referred to as the "strong CP problem". The Peccei-Quinn mechanism aims to solve this problem by introducing an additional chiral $U(1)$ symmetry [48]. Through its spontaneous symmetry breaking, the CP violating term vanishes dynamically, leaving one with a Nambu-Goldstone boson known as the axion [49, 50].

In the SUSY extension, the axino is introduced as the super-partner of the axion. A model including a light higgsino triplet ($\widetilde{\chi}_1^{\pm}$,$\widetilde{\chi}_2^0$,$\widetilde{\chi}_1^0$) decaying into an axino LSP [51] is proposed in the spirit of pursuing naturalness as well as axion/axino dark-matter [52, 53] under R-parity conservation.

The diagram of the models is shown in Figure 3(b). Higgsinos are produced by either of the four modes: $\widetilde{\chi}_1^{\pm}\widetilde{\chi}_1^{\mp}$, $\widetilde{\chi}_1^{\pm}\widetilde{\chi}_1^0$, $\widetilde{\chi}_1^{\pm}\widetilde{\chi}_2^0$, $\widetilde{\chi}_1^0\widetilde{\chi}_2^0$. The produced heavier higgsinos ($\widetilde{\chi}_1^{\pm}/\widetilde{\chi}_2^0$) are assumed to decay into the axino always via the lightest natural higgsino ($\widetilde{\chi}_1^0$). This is typically valid when wino and bino are reasonably decoupled to maintain approximate mass degeneracy among the higgsino triplet, and when the conventionally motivated range of the axion coupling constant is assumed [51]. A prompt $\widetilde{\chi}_1^0$ decay into an axino and a Z- or h-boson is considered in the search. The value of the branching ratio $\mathcal{B}(\widetilde{\chi}_1^0 \to Z\tilde{a})(= 1 - \mathcal{B}(\widetilde{\chi}_1^0 \to h\tilde{a}))$ is scanned over 25%, 50%, 75%, and 100% in the interpretation. The model is similar to $(\widetilde{H}, \widetilde{G})$, except that the LSP can be massive.

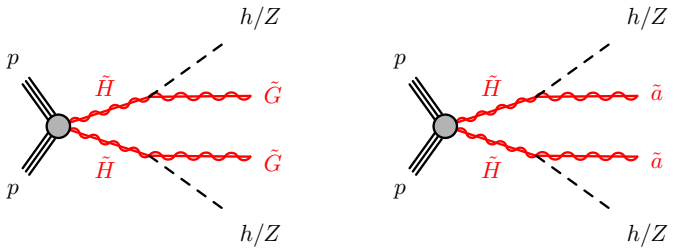

(a) $(\widetilde{H}, \widetilde{G})$ (b) $(\widetilde{H}, \tilde{a})$

Figure 3: Diagrams of signals considered in the (a) $(\widetilde{H}, \widetilde{G})$ and (b) $(\widetilde{H}, \tilde{a})$ models. In the $(\widetilde{H}, \widetilde{G})$ and $(\widetilde{H}, \tilde{a})$ model, the higgsino triplets $(\widetilde{\chi}_1^{\pm}, \widetilde{\chi}_2^0, \widetilde{\chi}_1^0)$ are collectively represented by $\widetilde{H}$.

3 ATLAS detector

The ATLAS experiment [55, 56] is a multipurpose detector with a forward–backward symmetric cylindrical geometry and nearly 4π coverage in solid angle.[8] It consists of an inner tracking detector surrounded by a thin superconducting solenoid providing a 2 T axial magnetic field, electromagnetic and hadron calorimeters, and a muon spectrometer.

The inner detector (ID) consists of pixel and microstrip silicon detectors covering the pseudorapidity range $|\eta| < 2.5$ and a transition radiation tracker covering $|\eta| < 2.0$. Outside the ID, a lead/liquid-argon (LAr) electromagnetic calorimeter (ECAL) and a steel/scintillator-tile hadronic calorimeter cover the $|\eta| < 3.2$ and $|\eta| < 1.7$ ranges, respectively. In the forward regions, a copper/LAr endcap calorimeter extends the coverage of hadronic measurements to $1.7 < |\eta| < 3.2$, while copper/LAr and tungsten/LAr forward calorimeters are employed for electromagnetic and hadronic measurements in the $3.1 < |\eta| < 4.9$ region. The muon spectrometer (MS) surrounds the calorimeters and comprises three layers of trigger and high-precision tracking chambers spanning $|\eta| < 2.4$ and $|\eta| < 2.7$, respectively. A magnetic field is

[8] ATLAS uses a right-handed coordinate system with its origin at the nominal interaction point (IP) in the centre of the detector and the z-axis along the beam pipe. The x-axis points from the IP to the centre of the LHC ring, and the y-axis points upwards. Cylindrical coordinates (r, ϕ) are used in the transverse plane, ϕ being the azimuthal angle around the z-axis. The pseudorapidity is defined in terms of the polar angle θ as $\eta = -\ln\tan(\theta/2)$. Angular distance is measured in units of $\Delta R \equiv \sqrt{(\Delta\eta)^2 + (\Delta\phi)^2}$.

Table 1: Summary of the production modes, final states, signal regions (SRs) used for the hypothetical tests and the branching ratio assumptions for the signal models targeted in the search. The notation and definition of the SRs are described in Section 6.2. $(\widetilde{W},\widetilde{B})$ and $(\widetilde{H},\widetilde{G})$ model are used for optimizing the selection, and the rest are considered for interpretation. The $(\widetilde{W},\widetilde{B})$ simplified models ($(\widetilde{W},\widetilde{B})$-SIM) discussed in Section 4.2.2 are also interpreted in order to compare with the ATLAS electroweakino search results [18, 19, 24, 54].

Model	Production	Final states	SRs simultaneously fitted	Branching ratio
$(\widetilde{W},\widetilde{B})$	$\widetilde{\chi}_1^{\pm}\widetilde{\chi}_1^{\mp}, \widetilde{\chi}_1^{\pm}\widetilde{\chi}_2^0$	WW, WZ, Wh	4Q-VV, 2B2Q-WZ, 2B2Q-Wh	$\mathcal{B}(\widetilde{\chi}_1^{\pm}\to W\widetilde{\chi}_1^0)=1$, $\mathcal{B}(\widetilde{\chi}_2^0\to Z\widetilde{\chi}_1^0)$ scanned.
$(\widetilde{H},\widetilde{B})$	$\widetilde{\chi}_1^{\pm}\widetilde{\chi}_1^{\mp}, \widetilde{\chi}_1^{\pm}\widetilde{\chi}_2^0$, $\widetilde{\chi}_1^{\pm}\widetilde{\chi}_3^0, \widetilde{\chi}_2^0\widetilde{\chi}_3^0$	WW, WZ, Wh, ZZ, Zh, hh	4Q-VV, 2B2Q-VZ, 2B2Q-Vh	$\mathcal{B}(\widetilde{\chi}_1^{\pm}\to W\widetilde{\chi}_1^0)=1$, $\mathcal{B}(\widetilde{\chi}_2^0\to Z\widetilde{\chi}_1^0)$ scanned, $\mathcal{B}(\widetilde{\chi}_3^0\to Z\widetilde{\chi}_1^0)=1-\mathcal{B}(\widetilde{\chi}_2^0\to Z\widetilde{\chi}_1^0)$
$(\widetilde{W},\widetilde{H})$	$\widetilde{\chi}_2^{\pm}\widetilde{\chi}_2^{\mp}, \widetilde{\chi}_2^{\pm}\widetilde{\chi}_3^0$	WW, WZ, Wh, ZZ, Zh, hh	4Q-VV, 2B2Q-VZ, 2B2Q-Vh	Determined from $(M_2,\mu,\tan\beta)$.
$(\widetilde{H},\widetilde{W})$	$\widetilde{\chi}_2^{\pm}\widetilde{\chi}_2^{\mp}, \widetilde{\chi}_2^{\pm}\widetilde{\chi}_2^0$, $\widetilde{\chi}_2^{\pm}\widetilde{\chi}_3^0, \widetilde{\chi}_2^0\widetilde{\chi}_3^0$	WW, WZ, Wh, ZZ, Zh, hh	4Q-VV, 2B2Q-VZ, 2B2Q-Vh	Determined from $(M_2,\mu,\tan\beta)$.
$(\widetilde{H},\widetilde{G})$	$\widetilde{\chi}_1^{\pm}\widetilde{\chi}_1^{\mp}, \widetilde{\chi}_1^{\pm}\widetilde{\chi}_1^0$, $\widetilde{\chi}_1^{\pm}\widetilde{\chi}_2^0, \widetilde{\chi}_1^0\widetilde{\chi}_2^0$	ZZ, Zh, hh	4Q-ZZ, 2B2Q-ZZ, 2B2Q-Zh	$\mathcal{B}(\widetilde{\chi}_1^0\to Z\widetilde{G})$ scanned.
$(\widetilde{H},\tilde{a})$	$\widetilde{\chi}_1^{\pm}\widetilde{\chi}_1^{\mp}, \widetilde{\chi}_1^{\pm}\widetilde{\chi}_1^0$, $\widetilde{\chi}_1^{\pm}\widetilde{\chi}_2^0, \widetilde{\chi}_1^0\widetilde{\chi}_2^0$	ZZ, Zh, hh	4Q-ZZ, 2B2Q-ZZ, 2B2Q-Zh	$\mathcal{B}(\widetilde{\chi}_1^0\to Z\tilde{a})$ scanned.
$(\widetilde{W},\widetilde{B})$ simplified models: $(\widetilde{W},\widetilde{B})$-SIM				
C1C1-WW	$\widetilde{\chi}_1^{\pm}\widetilde{\chi}_1^{\mp}$	WW	4Q-WW	$\mathcal{B}(\widetilde{\chi}_1^{\pm}\to W\widetilde{\chi}_1^0)=1$.
C1N2-WZ	$\widetilde{\chi}_1^{\pm}\widetilde{\chi}_2^0$	WZ	4Q-WZ, 2B2Q-WZ	$\mathcal{B}(\widetilde{\chi}_1^{\pm}\to W\widetilde{\chi}_1^0)=\mathcal{B}(\widetilde{\chi}_2^0\to Z\widetilde{\chi}_1^0)=1$.
C1N2-Wh	$\widetilde{\chi}_1^{\pm}\widetilde{\chi}_2^0$	Wh	2B2Q-Wh	$\mathcal{B}(\widetilde{\chi}_1^{\pm}\to W\widetilde{\chi}_1^0)=\mathcal{B}(\widetilde{\chi}_2^0\to h\widetilde{\chi}_1^0)=1$.

provided by a system of three superconducting air-core toroidal magnets with eight coils each. The field integral of the toroids ranges between 2.0 and 6.0 T m across most of the detector.

Events of interest are selected and collected by the ATLAS trigger system [57], consisting of a hardware-based first level trigger (L1) and a software-based high-level trigger (HLT). The L1 trigger is designed to reduce the 40 MHz collision rate to below 100 kHz, and the HLT further reduces this down to about 1 kHz, the rate at which events are recorded to disk.

4 Data and Monte Carlo simulation

4.1 Data sample

The data events used in the analysis are proton-proton collisions at $\sqrt{s}$ = 13 TeV, recorded during stable beam conditions at the LHC from 2015–2018. The collected dataset corresponds to an integrated luminosity of 139 fb^{-1} after applying the data quality criteria [58]. The primary dataset is collected by triggers targeting large missing transverse momentum [59]. Events are accepted when the $E_{\mathrm{T}}^{\mathrm{miss}}$ calculated at trigger level is greater than 70–110 GeV, with the threshold evolving with the increased instantaneous luminosity during the data taking period. The efficiency reaches approximately 100% for events with $E_{\mathrm{T}}^{\mathrm{miss}} > 200$ GeV as

reconstructed off-line, which is generally required in the search. Auxiliary data samples used to validate the background estimation were selected using triggers requiring at least one isolated electron, muon or photon [60, 61]. The thresholds were $p_{\mathrm{T}} > 24$ (26) GeV for electrons, $p_{\mathrm{T}} > 20$ (26) GeV for muons, and $p_{\mathrm{T}} > 120$ (140) GeV for photons in the data-taking during 2015 (2016–2018).

4.2 Monte Carlo simulation

Monte Carlo (MC) simulations are used to estimate the SM backgrounds and the signals contributing to the analysis regions. All of the generated events are propagated through the ATLAS detector simulation [62] based on GEANT4 4 [63]. Multiple proton-proton collisions in the same and neighboring bunch crossings (pile-up) are modeled by overlaying minimum-bias events simulated by PYTHIA 8.186 [64] with the A3 tune [65] and `NNPDF23lo` parton distribution function (PDF) set [66] onto the hard-scatter events.

The simulated events are processed with the same trigger and reconstruction algorithms as the data. The lepton and photon trigger efficiencies in simulation are corrected to match those in data using scale factors that depend on the p_{T} and η of the leptons and photons, as derived from the control samples [60, 61].

4.2.1 Standard Model Backgrounds

Events with a leptonically-decaying W and Z boson associated with hadron jets are simulated using the SHERPA v2.2.1 [67] generator. The matrix elements are calculated up to two partons at next-to-leading-order (NLO) accuracy and up to four jets at leading-order (LO) accuracy using the Comix [68] and OpenLoops [69, 70] generators. The NLO matrix elements of a given jet multiplicity are matched to the parton shower using a colour-exact variant of the MC@NLO algorithm [71]. Different jet multiplicities are then merged into an inclusive sample using an improved CKKW matching procedure [72, 73] which is extended to NLO accuracy using the MEPS@NLO prescription [74]. A 30 GeV threshold is employed for the merging procedure. `NNPDF30nnlo` PDF sets [75] are used with a tuning performed by the Sherpa authors. Prompt single-photon production, denoted as γ+jets, is simulated using the same configuration except that the generator version is SHERPA v2.2.2. The photons must be isolated according to a smooth-cone isolation criterion [76].

Samples of $t\bar{t}$ and single-top-quark ($t + X$) events are generated with POWHEG-BOX [77–80] v2 at NLO with the `NNPDF30nlo` PDF sets. The top mass is set to 172.5 GeV. For the $t\bar{t}$ generation, the h_{damp} parameter, which controls the p_{T} of the first additional emission beyond the Born configuration in POWHEG, is set to 1.5 times that of the top mass. This is to regulate the high-p_{T} emission recoiling against the $t\bar{t}$ system reproducing the data [81]. The parton shower, fragmentation, and underlying event are simulated using PYTHIA 8.230 with the `NNPDF23lo` PDF set and the A14 tune [82]. The decays of bottom and charm hadrons are performed by EvtGen v1.6.0 [83]. The diagram removal scheme [84] is employed to account for the interference between $t\bar{t}$ and single-top Wt production.

Events containing $t\bar{t}$ with additional heavy particles, such as $t\bar{t}+W/Z/h$, $t\bar{t}+WW$, $t\bar{t}t$ and $t\bar{t}t\bar{t}$, are collectively referred as $t\bar{t}+X$ in this paper. $t\bar{t}+W/Z$ is modeled by the MADGRAPH5_AMC@NLO v2.3.3 [85] generator at NLO accuracy with the `NNPDF30nlo` PDF [75] set, while $t\bar{t}+h$ is simulated by POWHEG v2.2. Both are interfaced with the PYTHIA 8.230 for parton showering. $t\bar{t}+h$ events are generated using the same setup as $t\bar{t}$ described above with the h mass is set to 125 GeV. $t\bar{t}+WW$, $t\bar{t}t$, and $t\bar{t}t\bar{t}$ are generated with

MadGraph5_aMC@NLO v2.2.2, interfaced to Pythia 8.210 using the A14 tune and the NNPDF23lo PDF set. The decays of bottom and charm hadrons are simulated using the EvtGen v1.2.0.

Di-boson production, including WW, WZ and ZZ, are collectively denoted as VV. Events of VV with semi-leptonic decays ($\ell\nu qq$, $\ell\ell qq$ and $\nu\nu qq$) are simulated with Sherpa v2.2.1 using the matrix elements up to one additional parton at NLO accuracy in QCD and up to three additional parton emissions at LO accuracy. Events with fully-leptonic VV decays are simulated with Sherpa v2.2.1 ($ZZ \to \nu\nu\nu\nu$) or v2.2.2 ($\ell\ell\ell\ell$, $\ell\ell\ell\nu$, $\ell\ell\nu\nu$ and $\ell\nu\nu\nu$) where all the processes at orders of $O(\alpha_{\text{EW}}^4, \alpha_S^2)$ and $O(\alpha_{\text{EW}}^6, \alpha_S^0)$ are taken into account, including the off-shell contributions and those mediated by Higgs bosons. The NNPDF30nnlo PDF set is used.

The production of Wh and Zh (collectively denoted as Vh) are generated using Powheg Box 2.2 interfaced with Pythia 8.186. The h mass is set to 125 GeV. NNPDF3 PDF set and the AZNLO tune are used.

Tri-boson production, including WWW, WWZ, WZZ and ZZZ, are collectively denoted as VVV. The $V(\to \ell\ell/\ell\nu/\nu\nu)V(\to qq)V(\to qq)$ processes are generated using MadGraph5_aMC@NLO v2.6.6 at LO, interfaced to Pythia 8.243 for modeling parton showers and hadronisation using the A14 tune. The NNPDF30lo PDF set is used.

Theoretical cross-sections are used to normalize the generated background samples. The $t\bar{t}$ sample is normalized to the cross-section predicted at NNLO in QCD including the resummation of next-to-next-to-leading-logarithmic (NNLL) soft-gluon terms calculated using Top++2.0 [86–92]. The cross-sections of single-top-quark t- and s-channel production are calculated using the Hathor v2.1 program [93, 94], while the Wt-channel followed the prescriptions from Refs. [95, 96]. VV and $t\bar{t}+W/Z$ production are normalized to the cross-sections calculated at NLO [97–99]. The cross-sections for the V+jets and γ+jets samples are calculated at NNLO [100]. The remaining samples, including the production of Vh, $V\gamma$, VVV, $t\bar{t}+WW$, tWZ, $t\bar{t}+h$, $t\bar{t}t$, and $t\bar{t}t\bar{t}$, are normalized to the cross-sections calculated at LO by the generators.

4.2.2 Signals

The $(\widetilde{W},\widetilde{B})$, $(\widetilde{H},\widetilde{B})$, $(\widetilde{W},\widetilde{H})$, $(\widetilde{H},\widetilde{W})$, and $(\widetilde{H},\tilde{a})$ models discussed in Section 2 are simulated by combining the "simplified model" signals in which a fixed production mode and decay chain are considered. Six sets of simplified model samples, derived as variants of the $(\widetilde{W},\widetilde{B})$ and $(\widetilde{H},\widetilde{B})$ models, are generated to cover the different final states:

- wino pair production, with each decaying into a bino LSP (denoted as $(\widetilde{W},\widetilde{B})$ simplified models or $(\widetilde{W},\widetilde{B})$-SIM):

$$\begin{aligned}
&\textbf{C1C1-WW:} && \widetilde{\chi}_1^{\pm}\widetilde{\chi}_1^{\pm} \to WW\,\widetilde{\chi}_1^0\widetilde{\chi}_1^0 && (\mathcal{B}(\widetilde{\chi}_1^{\pm} \to W\widetilde{\chi}_1^0) = 100\%)\\
&\textbf{C1N2-WZ:} && \widetilde{\chi}_1^{\pm}\widetilde{\chi}_2^0 \to WZ\,\widetilde{\chi}_1^0\widetilde{\chi}_1^0 && (\mathcal{B}(\widetilde{\chi}_1^{\pm} \to W\widetilde{\chi}_1^0) = \mathcal{B}(\widetilde{\chi}_2^0 \to Z\widetilde{\chi}_1^0) = 100\%)\\
&\textbf{C1N2-Wh:} && \widetilde{\chi}_1^{\pm}\widetilde{\chi}_2^0 \to Wh\,\widetilde{\chi}_1^0\widetilde{\chi}_1^0 && (\mathcal{B}(\widetilde{\chi}_1^{\pm} \to W\widetilde{\chi}_1^0) = \mathcal{B}(\widetilde{\chi}_2^0 \to h\widetilde{\chi}_1^0) = 100\%),
\end{aligned}$$

- neutral higgsino pair production, with each decaying into bino LSP (denoted as $(\widetilde{H},\widetilde{B})$-SIM):

$$\begin{aligned}
&\textbf{N2N3-ZZ:} && \widetilde{\chi}_2^0\widetilde{\chi}_3^0 \to ZZ\,\widetilde{\chi}_1^0\widetilde{\chi}_1^0 && (\mathcal{B}(\widetilde{\chi}_2^0 \to Z\widetilde{\chi}_1^0) = \mathcal{B}(\widetilde{\chi}_3^0 \to Z\widetilde{\chi}_1^0) = 100\%)\\
&\textbf{N2N3-Zh:} && \widetilde{\chi}_2^0\widetilde{\chi}_3^0 \to Zh\,\widetilde{\chi}_1^0\widetilde{\chi}_1^0 && (\mathcal{B}(\widetilde{\chi}_2^0 \to Z\widetilde{\chi}_1^0) = \mathcal{B}(\widetilde{\chi}_3^0 \to h\widetilde{\chi}_1^0) = 100\%)\\
&\textbf{N2N3-hh:} && \widetilde{\chi}_2^0\widetilde{\chi}_3^0 \to hh\,\widetilde{\chi}_1^0\widetilde{\chi}_1^0 && (\mathcal{B}(\widetilde{\chi}_2^0 \to h\widetilde{\chi}_1^0) = \mathcal{B}(\widetilde{\chi}_3^0 \to h\widetilde{\chi}_1^0) = 100\%).
\end{aligned}$$

The symbols C1, N2 and N3 in the model names represent $\widetilde{\chi}_1^{\pm}$, $\widetilde{\chi}_2^0$ and $\widetilde{\chi}_3^0$ respectively. These samples are used for modeling event kinematics for each final state; the $(\widetilde{W}, \widetilde{B})$-SIM samples are used for events containing WW, WZ or Wh, while $(\widetilde{H}, \widetilde{B})$-SIM samples are employed to model events with ZZ, Zh or hh. A re-weighting is applied to account for the production cross-section and the $\widetilde{\chi}_{\text{heavy}}$ branching ratios considered in the model. The underlying assumption for the method is that the event kinematics depend only on $m(\widetilde{\chi}_{\text{light}})$ and $m(\widetilde{\chi}_{\text{heavy}})$, instead of the production modes, type of LSPs, and other MSSM variables such as $\tan\beta$. This is confirmed to be valid in the phase space considered in the analysis using generator-level samples.

The $(\widetilde{W}, \widetilde{B})$-SIM models are also considered in the limit interpretation in order to compare with previous ATLAS searches, as these have been most commonly studied [18, 20–24, 27–32]. For the $(\widetilde{H}, \widetilde{G})$ model, a dedicated sample is generated with all of the production modes $(\widetilde{\chi}_1^{\pm}\widetilde{\chi}_1^{\mp}, \widetilde{\chi}_1^{\pm}\widetilde{\chi}_1^0, \widetilde{\chi}_1^{\pm}\widetilde{\chi}_2^0, \widetilde{\chi}_1^0\widetilde{\chi}_2^0)$ included.

All of the signal samples are simulated using the LO matrix elements with up-to two extra partons using MadGraph5_aMC@NLO v2.6.2. The events are subsequently interfaced with Pythia 8.230 [101] for simulating parton showering and hadronization. The A14 tune [82] of Pythia is used with the `NNPDF23lo` PDF set. The mass of the SM-like Higgs boson is set to 125 GeV.

Decays of the produced electroweakinos are simulated using Pythia. As the performance of the boosted W/Z-boson tagging is known to be sensitive to the boson polarization [34], W/Z bosons from the electroweakino decays are carefully modeled either using MadSpin v2.7.3 [102, 103] or by re-weighting the helicity angle distribution such that the overall cross-section remains unchanged. W/Z-bosons are typically longitudinally polarized when $\Delta m(\widetilde{\chi}_{\text{heavy}}, \widetilde{\chi}_{\text{light}}) > 400$ GeV is considered. The decays of bottom and charm hadrons are performed by EvtGen v1.2.0.

The signal cross-sections are computed at NLO in the strong coupling constant, adding the resummation of soft gluon emission at next-to-leading-logarithm (NLL) accuracy. The `PDF4LHC15_mc` PDF set is used following the recommendations in Ref. [104]. Assuming a mass of 800 GeV, the calculated cross-section for wino-like (higgsino-like) chargino pair production is 2.21 (0.63) fb, and 4.76 (1.12) fb for wino-like (higgsino-like) chargino-neutralino production. For neutral higgsino pair production, the corresponding cross-section is 0.59 fb.

5 Event reconstruction

The primary reconstructed objects used in the analysis are large-radius jets (large-R jets, represented by J). These are reconstructed from locally calibrated topo-clusters [105] using the anti-k_t algorithm [106] implemented in the FastJet package [107] with the radius parameter $R = 1.0$. A trimming algorithm [108] is applied to mitigate effects of pile-up and soft radiation. The constituents of each jet are reclustered with the k_t algorithm [109] into $R = 0.2$ subjets, and the subjets are removed if $p_{\text{T}}^{\text{subjet}}/p_{\text{T},J} < 0.05$ where $p_{\text{T}}^{\text{subjet}}$ and $p_{\text{T},J}$ are the transverse momenta of the subjet and the large-R jet, respectively. The jet mass, m_J, is calculated based on the combined mass prescription [110] to achieve the best mass resolution, which is given by the weighted sum of masses computed using only the calorimeter information and with tracking information included. The p_{T} and mass scales are calibrated using simulation, followed by an in-situ calibration [111] to correct for residual difference between data and MC. Large-R jets used in the analysis are selected with $p_{\text{T}} > 200$ GeV, $|\eta| < 2.0$, and $m_J > 40$ GeV.

Track jets are used to identify sub-jets inside the large-R jets that contain b-hadrons. These are reconstructed with the ID tracks by using the anti-k_t algorithm with a sliding radius parameter $R = 30\ \text{GeV}/p_{\text{T}}$ truncated at 0.02 and 0.4 [112]. b-tagging is applied for track jets satisfying $p_{\text{T}} > 20$ GeV and $|\eta| < 2.5$. The MV2c10 algorithm [113] is used, a multivariate discriminator that utilizes track impact parameters, the presence of secondary vertices, and the trajectories of b- and c- hadrons inside the jet. A working point is chosen such that b-jets from simulated $t\bar{t}$ events are identified with an 85% efficiency, with rejection factors of 3 against charm-quark jets and 33 against jets originated from other light-flavor quarks or gluons [113]. Efficiency correction factors are applied to simulated samples to account for the efficiency difference observed between in the MC and data in dedicated measurement regions in which $t\bar{t}$ samples [113, 114] are used for b-jets and mis-tagged c-jets, and Z + jets samples for the light-flavor mis-tagged jets [115].

The b-jet multiplicity for a given large-R jet is defined by the number of b-tagged track jets that are contained by the large-R jet within $\Delta R < 1.0$ where ΔR is the angular distance between the two jet axes.

Two types of boosted boson tagging are employed for the preselected large-R jets to identify the SM boson decays; W_{qq} (Z_{qq})-tagging targeting $W(Z) \to qq$, and Z_{bb} (h_{bb})-tagging targeting $Z(h) \to bb$. The W_{qq} (Z_{qq})-tagging utilizes cuts on m_J, the energy correlation function D_2, and the track multiplicity n_{trk} [34, 116]. In order to maintain orthogonality with the Z_{bb} (h_{bb})-tagging, the b-jet multiplicity of the large-R jet is required to be less than two. The D_2 variable is defined as a ratio of two- and three-point energy correlation functions [117, 118] based on the energies and pairwise angular distances of particles within a jet. n_{trk} is the number of tracks that are ghost-associated to the large-R jet before the applying the trimming. While the upper cut in n_{trk} is fixed, the cut values on m_J and D_2 are smoothly shifted as a function of p_{T} to maximize the rejection for typical single-parton initiated jets, maintaining a flat efficiency for signal jets that contain the decay products of W (Z) $\to qq$. The selections are optimized separately for targeting W and Z, and V_{qq}-tagging is defined by the selection passing either the W_{qq}- or Z_{qq}-tagging. The same cut values are applied on m_J and D_2 as the "50% efficiency W/Z tagger" in Ref. [116], however a loosened n_{trk} cut, from ≤ 26 to ≤ 32 (34) for the W_{qq} (Z_{qq})-tagging, is applied to achieve the optimum sensitivity for the analysis and better modeling in MC. The efficiency correction factors are re-derived according to the refinement, using the similar methodology described in Ref. [116]. A correction factor of 0.85–0.95 is typically obtained. The performance of the W_{qq}- and Z_{qq}-tagging is summarized in Figure 4. For a sample of pre-selected large-R jets ($p_{\text{T}} > 200$ GeV, $|\eta| < 2.0, m_J > 40$ GeV), the tagging efficiency is about 50% for the signal jets originated from electroweakino decays, [9] while the background rejection is typically about 10 (40) at $p_{\text{T}} = 200$ (1000) GeV per jet in $Z(\to \nu\nu)$ + jets events.

The Z_{bb} (h_{bb}) tagging is applied for large-R jets containing exactly two b-jets inside (denoted as J_{bb}) by applying a jet mass window cut that selects the peak consistent with Z (h)-bosons. The jet mass is corrected by adding the momentum of the highest-p_{T} muon identified inside the large-R jet in order to improve the resolution of the mass peak. The Z_{bb} (h_{bb})-tagging requires the jet mass to satisfy 70 (100) GeV $< m_J <$ 100 (135) GeV.

The analysis also uses reconstructed electrons, muons (collectively referred to as "leptons"), photons and small-radius (small-R) jets for kinematic selection, validation of the background estimation, and the $E_{\text{T}}^{\text{miss}}$ computation. Electron candidates are reconstructed from energy clusters that are consistent with electromagnetic showers in the ECAL and are matched to tracks in the ID, which are calibrated in-situ using $Z \to ee$ sample [119]. Muon candidates in the detector are typically reconstructed by matching tracks formed in the MS and ID, and they are calibrated in-situ using $Z \to \mu\mu$ and $J/\psi \to \mu\mu$ samples [120]. Small-R jet candidates are reconstructed from particle-flow objects [121] calibrated at the electromagnetic

[9] The corresponding efficiency for the "50% efficiency W/Z tagger" [116] is 35–40% for this particular set of jet sample

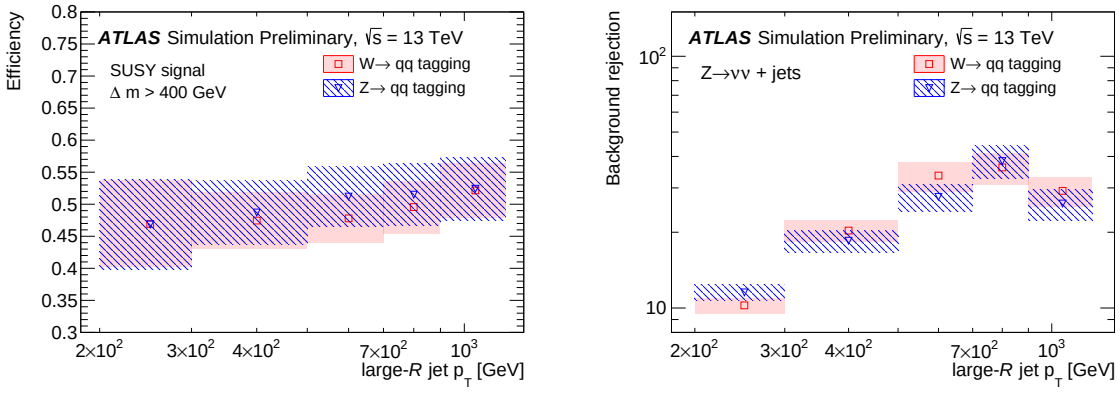

(a) Efficiency

(b) Rejection factor

Figure 4: (a) The W_{qq} (Z_{qq})-tagging efficiency for boson jets arising from electroweakino decays and (b) the background rejection factor (inverse of the efficiency). The W_{qq}- and Z_{qq}-tagging is shown in the red and blue bands respectively. The signal jet efficiency is evaluated using a sample of pre-selected large-R jets ($p_{\mathrm{T}} > 200$ GeV, $|\eta| < 2.0, m_J > 40$ GeV) in the simulated $(\widetilde{W}, \widetilde{B})$-SIM signal events with $\Delta m(\widetilde{\chi}_{\mathrm{heavy}}, \widetilde{\chi}_{\mathrm{light}}) \geq 400$ GeV that are matched with generator-level W/Z-bosons by $\Delta R < 1.0$. The rejection factor is calculated using pre-selected large-R jets in the sample of simulated $Z(\rightarrow \nu\nu)$ + jets events, dominated by initial state radiation (ISR) jets. The efficiency correction factors are applied for both the signal efficiency and background rejection.

scale using the anti-k_t algorithm with a radius parameter of $R = 0.4$. After subtracting the expected energy contribution from pileup following the jet area technique [122], the jet energy scale and resolution are corrected to particle level using MC simulation as well as by the *in-situ* calibration using Z+jets, γ+jets, and multi-jet events [123]. Photon candidates are reconstructed either by electromagnetic clusters with no ID tracks matched or e^+e^- pairs from photon conversions induced by the ID material [119].

Reconstructed electrons, muons, small-R jets, and photons are subject to two identification criteria: the looser "baseline" criteria and the tighter "signal" criteria. The baseline objects are used for the $E_{\mathrm{T}}^{\mathrm{miss}}$ computation, event cleaning, and the overlap removal procedure that resolves ambiguities between reconstructed objects described below. Baseline electrons are required to have $p_{\mathrm{T}} > 4.5$ GeV and $|\eta| < 2.47$, and pass the *Loose* criteria of the likelihood-based identification [119]. Baseline muons are required to have $p_{\mathrm{T}} > 3$ GeV and $|\eta| < 2.7$ to meet the *Medium* identification defined in Ref [124]. To suppress the contributions from pile-up, baseline leptons are also required to have a trajectory consistent with the primary vertex, i.e. $|z_0 \sin\theta| < 0.5$ mm.[10] Baseline small-R jets must have $p_{\mathrm{T}} > 30$ GeV and $|\eta| < 4.5$. Baseline photons must pass the *Tight* identification criteria [119] in addition to satisfying $p_{\mathrm{T}} > 50$ GeV and $|\eta| < 2.4$.

To prevent the reconstruction of a single particle as multiple objects, an overlap-removal procedure is performed with the baseline leptons, photons, and jets in the following order. Any electron sharing an ID track with a muon or the other electrons is removed, such that only the highest-p_{T} electron is kept when multiple electrons share the same ID track. Photons around the remaining electrons and muons are removed if they are separated by $\Delta R < 0.4$. Next, small-R jets are removed if they satisfy $\Delta R < 0.2$ with respect to the remaining electron or photon, or $\Delta R < 0.4$ with respect to the muons when the jets

[10] The transverse impact parameter, d_0, is defined as the distance of closest approach in the transverse plane between a track and the beam-line. The longitudinal impact parameter, z_0, corresponds to the z-coordinate distance between the point along the track at which the transverse impact parameter is defined and the primary vertex.

have fewer than three associated tracks with $p_{\mathrm{T}} > 500$ MeV. The leptons (photons) are removed if they are nearby a remaining small-R jet to within $\Delta R < \min(0.4, 0.04 + 10\ \mathrm{GeV}/p_{\mathrm{T},\ell})$ ($\Delta R < 0.4$). Finally, large-R jets are removed if they are separated by $\Delta R < 1.0$ from any remaining electrons.

The missing transverse momentum and the magnitude $E_{\mathrm{T}}^{\mathrm{miss}}$ are calculated as the negative of the vectorial sum of the transverse momenta of all the baseline leptons, photons and small-R jets calibrated to the respective energy scale, and an additional "soft term" constructed from tracks originating from the primary vertex that are not associated to any of the baseline objects [125].

Signal objects are defined by additional stringent criteria applied, used in event selections to ensure a high selection purity. Signal leptons and photons are used only for validating the background estimation. Signal electrons and muons must satisfy $p_{\mathrm{T}} > 10$ GeV. Additionally, the *Tight* identification criteria are required for signal electrons. To reduce the contribution from non-prompt decays of heavy-flavour hadrons, the significance of the transverse impact parameter is required to satisfy $|d_0/\sigma(d_0)| < 5(3)$ for signal electrons (muons). Isolation selection is further imposed to suppress the residual mis-identified leptons originating from jets. The *Tight* (*HighPtCaloOnly*) working point defined in Ref. [119] is used for signal electrons with $p_{\mathrm{T}} < 200$ GeV ($p_{\mathrm{T}} > 200$ GeV), and the *Tight* working point defined in Ref. [120] is applied for signal muons. Signal small-R jets are selected within $|\eta| < 2.8$ and satisfy the *Tight* quality criteria of the track-based jet vertex tagger [122, 126] when $p_{\mathrm{T}} < 120$ GeV and $|\eta| < 2.5$ in order to suppress jets originating from pileup. Signal photons are defined as baseline photons with $p_{\mathrm{T}} > 200$ GeV.

6 Event selection

6.1 Common pre-selection

As described below, a common pre-selection is used for defining the signal regions (SRs), as well as the control regions (CRs) and validation regions (VRs) used for background estimation.

After the trigger requirement discussed in Section 4.1, both the data and MC events are required to have at least one reconstructed vertex that is associated with two or more tracks of transverse momentum $p_{\mathrm{T}} > 500$ MeV. The primary vertex of each event is selected as the vertex with the largest $\sum p_{\mathrm{T}}^2$ of associated tracks [127].

A set of event cleaning criteria follows to ensure the quality of the energy measurement as well as to veto non-collision backgrounds. Events with baseline muons consistent with cosmic muons ($|z_0| > 1$ mm or $|d_0| > 0.2$ mm) are removed. To avoid pathological $E_{\mathrm{T}}^{\mathrm{miss}}$ reconstruction, events are also vetoed if any baseline jet is pointing to modules of the tile hadronic calorimeter that were not operational during the data taking, or if any baseline muons suffer from a poor momentum measurement ($\sigma(q/p)/(q/p) > 0.4$ where q/p is the measured charge divided by momentum and $\sigma(q/p)$ is its uncertainty). Beam induced background is one of the major non-collision backgrounds where particles (typically muons) generated by the interaction between the beam and the upstream collimators directly hit the detector materials. Particular care is needed for this background since it can cause high energy jet-like signatures and, correspondingly, large spurious $E_{\mathrm{T}}^{\mathrm{miss}}$ [128]. Events with baseline jets failing the *Loose* cleaning [129] are removed. Further cleaning is applied for events with no baseline leptons and photons by requiring consistency between the $E_{\mathrm{T}}^{\mathrm{miss}}$ and the alternative $E_{\mathrm{T,track}}^{\mathrm{miss}}$, which is computed using only the good-quality ID tracks associated with the primary vertex. While those events satisfy $E_{\mathrm{T}}^{\mathrm{miss}} > 200$ GeV from the trigger requirements, $E_{\mathrm{T,track}}^{\mathrm{miss}} > 75$ GeV and $\Delta\phi(E_{\mathrm{T}}^{\mathrm{miss}}, E_{\mathrm{T,track}}^{\mathrm{miss}}) < 2.0$ are applied in the cleaning procedure.

Finally, events are required to contain at least two large-R jets. Events with three or more large-R jet are not vetoed in the analysis in order to be as inclusive as possible in model coverage, however the event selection is always applied based on the two highest-p_{T} large-R jets.

6.2 Signal region selection

After the pre-selection, events with no baseline leptons are selected. Two orthogonal signal region categories, 4Q and 2B2Q, are defined respectively based on the absence or presence of a large-R jet containing exactly two b-tagged track jets (J_{bb}), to target the $qqqq$ and $bbqq$ final states respectively.

Boson tagging is required for the two leading large-R jets, which provides the most powerful background rejection in the analysis. The two leading large-R jets must pass the V_{qq}-tagging ($n(V_{qq}) = 2$) in SR-4Q. On the other hand, SR-2B2Q requires J_{bb} to satisfy the Z_{bb} (h_{bb})-tagging, while the other jet (denoted as J_{qq}) must pass the V_{qq}-tagging criteria. Multiple SRs are defined in each SR category to target the different final states of the signal processes. The WW (ZZ) region in SR-4Q requires both leading large-R jets to pass the W_{qq} (Z_{qq})-tagging, while the WZ region is defined to contain events with at least one W_{qq}-tagged and at least one Z_{qq}-tagged jet. The inclusive bin VV, the logical union of WW, WZ and ZZ, is designed to cover the signals that can have various $\widetilde{\chi}_{\mathrm{heavy}}$ branching ratios into W relative to Z. Similarly, the 2B2Q category accommodates the WZ/ZZ/Wh/Zh region varying by W_{qq}- versus Z_{qq}-tagging or Z_{bb}- versus h_{bb}-tagging. The VZ (Vh) region serves as the inclusive SR defined by the logical union of WZ and ZZ (Wh and Zh). The SR segmentation is summarized in Table 2 and illustrated as a schematic in Figure 5. In total, four and six SRs are defined in SR-4Q and SR-2B2Q, respectively. SR-4QXX, SR-2B2QXZ and SR-2B2QXh (X := W/Z/V) are mutually orthogonal, and are statistically combined according to the models considered in Table 1.

Table 2: Definition of each SR in the 4Q and 2B2Q category. $n(W_{qq})$, $n(Z_{qq})$, $n(V_{qq})$, $n(Z_{bb})$, and $n(h_{bb})$ are respectively the number of large-R jets passing the W_{qq}-, Z_{qq}-, V_{qq}-, Z_{bb}-, and h_{bb}-tagging of two leading large-R jets. Note that SR-4Q-WZ requires $n(W_{qq}), n(Z_{qq}) \geq 1$ instead $n(W_{qq}), n(Z_{qq}) = 1$ due to the fact that the selection of W_{qq}- and Z_{qq}-tagging are not exclusive. The overlap and the segmentation between the SRs are illustrated in Fig 5.

	$n(W_{qq})$	$n(Z_{qq})$	$n(V_{qq})$	$n(Z_{bb})$	$n(h_{bb})$
4Q-WW	$= 2$	-	$= 2$	$= 0$	$= 0$
4Q-WZ	≥ 1	≥ 1	$= 2$	$= 0$	$= 0$
4Q-ZZ	-	$= 2$	$= 2$	$= 0$	$= 0$
4Q-VV	-	-	$= 2$	$= 0$	$= 0$
2B2Q-WZ	$= 1$	-	$= 1$	$= 1$	$= 0$
2B2Q-ZZ	-	$= 1$	$= 1$	$= 1$	$= 0$
2B2Q-Wh	$= 1$	-	$= 1$	$= 0$	$= 1$
2B2Q-Zh	-	$= 1$	$= 1$	$= 0$	$= 1$
2B2Q-VZ	-	-	$= 1$	$= 1$	$= 0$
2B2Q-Vh	-	-	$= 1$	$= 0$	$= 1$

Finally, a series of background rejection cuts are applied to further suppress the main SM backgrounds at this stage: $Z(\rightarrow \nu\nu)$ + jets, $W(\rightarrow \ell\nu)$ + jets, and $t\bar{t}$. To reject backgrounds including top-quarks, b-jets that do not originate from the boosted boson candidates are vetoed. This is done by requiring $n_{b-\mathrm{jet}}^{\mathrm{unmatched}} = 0$,

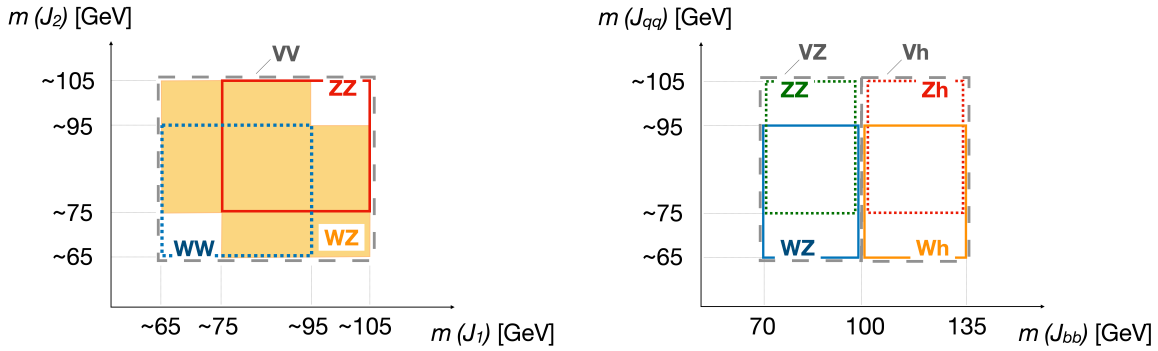

(a) SR-4Q

(b) SR-2B2Q

Figure 5: The SR segmentation illustrated as a function of the masses of the two leading large-R jets. (a) In SR-4Q, both jets are required to pass the W_{qq}- or Z_{qq}-tagging. (b) In SR-2B2Q, one of the two jets is required to contain exactly two b-tagged track jets (J_{bb}) while the other is with at most one (J_{qq}). The mass of J_{bb} is required to be consistent with Z (70 – 100 GeV) or h (100 – 135 GeV), while the J_{qq} is required to pass the W_{qq}- or Z_{qq}-tagging. Note that the mass window cuts of the W_{qq}-/Z_{qq}-tagging shown in the plot only indicate the typical values, while variable cut values along p_{T} are applied in the analysis. for which the typical cut values are indicated. The inclusive SRs, defined by the logical union of a few mutually overlapping SRs, are indicated by the gray dashed lines.

where $n_{b-\mathrm{jet}}^{\mathrm{unmatched}}$ denotes the number of b-tagged track jets that are not matched with any of the two leading large-R jets by $\Delta R < 1.0$. For the 4Q category, the total number of b-tagged track jets in the event ($n_{b-\mathrm{jet}}$) is limited to be less than two in order to further suppress the $t\bar{t}$ background. The effective mass variable, m_{eff}, defined as the scalar sum of p_{T} of the leading two large-R jets and $E_{\mathrm{T}}^{\mathrm{miss}}$, is used to select events with hard kinematics together with $E_{\mathrm{T}}^{\mathrm{miss}}$. Selections of $E_{\mathrm{T}}^{\mathrm{miss}} > 300$ (200) GeV and $m_{\mathrm{eff}} > 1300$ (1000) GeV are applied in the 4Q (2B2Q) regions. Event shape information is also useful to discriminate the signals from the backgrounds. Signal events have a relatively spherical shape, where the jets tend to be isolated from $E_{\mathrm{T}}^{\mathrm{miss}}$, indicating that the heavy electroweakinos are produced relatively at rest. Background events, meanwhile, have a higher chance of containing a jet aligned with W/Z due to the emission of collinear radiation (in Z + jets and W + jets) or boosted top decays (in $t\bar{t}$). An angular variable $\min \Delta\phi(E_{\mathrm{T}}^{\mathrm{miss}}, j)$, the minimum azimuthal angle difference between $E_{\mathrm{T}}^{\mathrm{miss}}$ and any signal small-R jets, is required to be greater than 1.0 for both SR categories. The use of small-R jets is motivated for effectively identifying the low-p_{T} jets as well as providing better resolution in terms of the alignment with $E_{\mathrm{T}}^{\mathrm{miss}}$. In 2B2Q, the stransverse mass variable m_{T2} [130, 131] is also used, constructed by assigning each of the two leading large-R jets to the visible particle legs. A selection of $m_{\mathrm{T2}} > 250$ GeV is found to effectively suppress the SM backgrounds, particularly $t\bar{t}$ which presents a kinematic cut-off at $m_{\mathrm{T2}} \sim 200$ GeV, driven by the top mass constraint.[11]

The cut values of the kinematic selection are equivalent within the SR-4Q and SR-2B2Q categories. The selection criteria that define the SR-4Q, SR-2B2Q-Wh, and SR-2B2Q-Vh regions are driven by optimizing the sensitivity to the $(\widetilde{W}, \widetilde{B})$ model with $(m(\widetilde{\chi}_1^{\pm}), m(\widetilde{\chi}_1^0)) \approx (800, 100)$ GeV, while those for SR-2B2Q-WZ, SR-2B2Q-ZZ and SR-2B2Q-VZ are determined by optimizing the sensitivity to the $(\widetilde{H}, \widetilde{G})$ model with $m_{\widetilde{\chi}_1^0}$ of about 800 GeV. The discovery significance is used as the metric of sensitivity. The obtained cuts are also confirmed to be nearly optimal for the other signal models.

[11] The hypothetical missing particle mass is set to 100 GeV and this offset is subtracted from the calculated m_{T2}, although the dependency on the choice of missing particle mass is very small.

7 Background estimation

The main SM background process in the SRs is $Z(\to \nu\nu)$+jets ($\sim$ 50%), followed by $W(\to \ell\nu)$+jets (15–20%), and VV (10–20%). The rest consists of VVV events in SR-4Q (5–10%), or $t\bar{t}$, single-top and $t\bar{t}+X$ events in SR-2B2Q (10–20%).

The estimation strategy varies between the "reducible" and "irreducible" backgrounds. The irreducible backgrounds in this search are due to SM events including at least two hadronic $W/Z/h$ decays and large $E_{\mathrm{T}}^{\mathrm{miss}}$ from high-p_{T} neutrinos. These consist of VVV and $t\bar{t}+X$, and are estimated using MC simulation.

The reducible backgrounds are all that remain, including the dominant $Z(\to \nu\nu)$ + jets production. These backgrounds are characterized by the presence of at least one large-R jet that originates from a process other than a $W/Z \to qq$ decay, referred to as a "fake boson jet". The fake boson jets are typically caused by two collimated high-p_{T} initial-state radiation (ISR) jets clustered together as a single large-R jet. A semi data-driven method is used to estimate the reducible backgrounds; a control region (CR0L) [12] is defined in the adjacent phase space to a SR, where the MC sample is normalized to the CR data. The SR expectation is obtained using the corrected MC sample, assuming the modeling of the SR/CR0L yield ratio ("0L transfer factor") is reliable. This assumption is tested in a number of validation regions (VR) in data. A CR0L is defined for each 4Q and 2B2Q category by reversing the V_{qq}-tagging requirement on one of the two leading large-R jets in the SR, denoted as CR0L-4Q and CR0L-2B2Q, respectively. The contribution of multi-jet and non-collision backgrounds are found to be negligible using the data-driven methods or based on the estimation in the similar phase space carried out in Ref. [132].

The following sub-sections discuss the methodology and results for the irreducible and reducible background estimations.

7.1 Irreducible background estimation

VVV ($t\bar{t}+X$) events account for at most 10% of the total background in SR-4Q (SR-2B2Q), and are negligible in SR-2B2Q (SR-4Q). Given their minor contribution, these backgrounds are estimated directly using the MC predictions and assigned conservative uncertainties.

The dominant $t\bar{t}+X$ component in SR-2B2Q is $t\bar{t}(\to b\ell\nu bqq)+Z(\to \nu\nu)$. To validate the MC modeling, a dedicated validation region VRTTX is defined in a 3-lepton region populated by $t\bar{t}(\to b\ell\nu bqq)+Z(\to \ell\ell)$. The selections are summarized in Table 3. Exactly three baseline and signal leptons are required, with the leading lepton of $p_{\mathrm{T}} > 30$ GeV firing the single-lepton trigger. At least one large-R jet is required in the event, which must contain exactly two b-tagged track jets. No further kinematic cuts are applied in order to maintain sufficient data sample size in the region. The $t\bar{t}+X$ purity in this region is about 70%. 68 data events are observed in VRTTX, while 46.5 events are predicted by MC simulation (31.5 by $t\bar{t}+X$, 12.1 by VV, and 2.9 by the others). A 70% uncertainty on $t\bar{t}+X$ normalization is therefore assigned to fully cover the observed discrepancy, which has a small impact on the total background estimation, given the minor contribution in the SRs.

VVV contribution to SR-4Q is dominantly from $VV(\to qqqq)+Z(\to \nu\nu)$ processes. VVV has only recently been observed at the LHC in a phase space with low data sample size [133, 134]. As the data sample size are insufficient in this region and loosening the selection leads to poor VVV purity, no control or validation regions are designed and this background is estimated directly from the MC prediction.

[12] "0L" stands for regions with zero baseline lepton.

7.2 Reducible background estimation

The CR0L-4Q is defined by the same selection as SR-4Q-VV except that one of the two leading large-R jets must fail the V_{qq}-tagging, and the CR0L-2B2Q is constructed as the logical union of SR-2B2Q-VZ and SR-2B2Q-Vh with the J_{qq} failing the V_{qq}-tagging. For the reducible backgrounds, the extrapolation from a CR0L to the SR is mainly characterized by the V_{qq}-tagging response of a fake boson jet. In order to maintain sufficient data sample size and to suppress signal contamination, the m_{eff} selection and the J_{bb} mass window cut for CR0L-2B2Q are loosened with respect to the SR, from $m_{\text{eff}} > 1000$ GeV to $m_{\text{eff}} > 900$ GeV and from $70 < m(J_{bb}) < 135$ GeV to $70 < m(J_{bb}) < 150$ GeV. The signal contamination in CR0L-4Q and CR0L-2B2Q is evaluated using the $(\widetilde{W}, \widetilde{B})$-SIM and $(\widetilde{H}, \widetilde{G})$ samples. While a contribution of up to 15% (24%) of the expected backgrounds in CR0L-4Q (CR0L-2B2Q) can be caused by the non-excluded signals, the introduced bias in the estimation is still smaller than the total uncertainty in the SRs and VRs, and therefore has a small impact on the final sensitivity. The selections are summarized in Table 3, and the relation with the SR is illustrated in Figure 6.

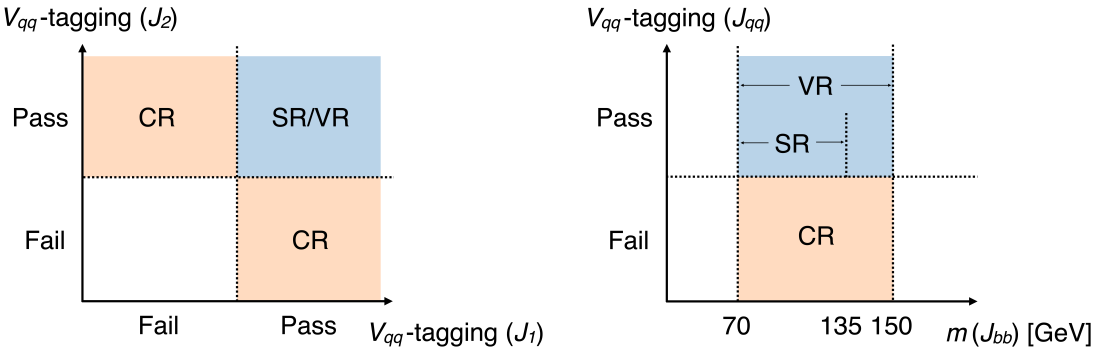

(a) 4Q

(b) 2B2Q

Figure 6: Schematics illustrating the relation between the signal regions (SRs), validation regions (VRs) and control regions (CRs) in the (a) 4Q and (b) 2B2Q categories. A CR is constructed by inverting the V_{qq}-tagging requirement of one of the two leading large-R jets in the corresponding SR (VR). In 2B2Q, the J_{bb} mass window cut in the CRs and VRs is loosened. See Table 3 for details.

One advantage of this CR0L definition is that all physics processes contributing to the background (Z + jets, W + jets, $t\bar{t}$...) have comparable 0L transfer factors. This is because the fake boson jets have similar origins and kinematics, and therefore the same boson tagging efficiency, confirmed by the simulation. Consequently, they can be treated as a single combined component with a common normalization factor assigned to correct their normalizations at once. The normalization is performed in 4Q and 2B2Q separately with an independent normalization factor, based on the "background-only" fits described in Section 9.1.

The MC modeling of the 0L transfer factor is essential to the estimation. Data events with exactly one lepton or one photon are utilized for the validation. This is motivated by the fact that the main background in the respective region, $Z(\to \nu\nu)$ + jets (SR/CR0L), $W(\to \ell\nu)$ + jets (1-lepton region) and γ + jets (1-photon region) production have the similar ISR jet kinematics, and relative composition with respect to the other minor backgrounds when a compatible kinematic phase space is chosen. The 1-lepton (1-photon) region corresponding to CR0L and SR is constructed, denoted as CR1L(1Y) and VR1L(1Y) respectively. The

level of data-vs-MC agreement on the ratio VR1L(1Y)/CR1L(1Y) ("1L(1Y) transfer factor") is verified as the proxy to the MC modeling on the 0L transfer factor.

The selections applied for VR(CR)1L and VR(CR)1Y are listed in Table 3. The VR(CR)1L is defined by requiring exactly one baseline lepton and a signal lepton with $p_{\mathrm{T}} > 30$ GeV that fires the single-lepton trigger. In addition, $E_{\mathrm{T}}^{\mathrm{miss}} > 50$ GeV is required to suppress contributions from QCD multi-jet events with badly measured $E_{\mathrm{T}}^{\mathrm{miss}}$. The VR(CR)1Y has exactly one baseline and signal photon firing the single-photon trigger, and vetoes events with at least one baseline lepton. For both VR(CR)1L and VR(CR)1Y, at least two large-R jets are requested, and the events are split into the 4Q and 2B2Q categories based on the presence of J_{bb}. A similar b-jet veto strategy is applied as in the SRs and the CR0L bins; $n_{b-\mathrm{jet}}^{\mathrm{unmatched}} = 0$ in all the regions, $n_{b-\mathrm{jet}} \leq 1$ in the 4Q regions. A stricter veto of $n_{b-\mathrm{jet}} = 0$ is applied in CR(VR)1L-4Q to suppress the large single-top contribution relative to the other 4Q regions.

The kinematic selection in the 1L (1Y) regions is applied with replacing $E_{\mathrm{T}}^{\mathrm{miss}}$ into $p_{\mathrm{T}}(W)$ ($p_{\mathrm{T}}(\gamma)$) in the variables. This is to ensure that compatible phase space is probed between $Z(\to \nu\nu)$ + jets in SR/CR0L, $W(\to \ell\nu)$ + jets in VR1L/CR1L, and γ + jets in VR1Y/CR1Y, as $E_{\mathrm{T}}^{\mathrm{miss}}$ in $Z(\to \nu\nu)$ + jets events typically represents p_{T} of the Z-boson. $p_{\mathrm{T}}(W)$ is defined as the vector sum of the p_{T} of lepton and $E_{\mathrm{T}}^{\mathrm{miss}}$ in the 1L regions. $E_{\mathrm{T}}^{\mathrm{miss}}$, $p_{\mathrm{T}}(W)$ and $p_{\mathrm{T}}(\gamma)$ are collectively referred to as $p_{\mathrm{T}}(V)$. The $\min \Delta\phi(E_{\mathrm{T}}^{\mathrm{miss}}, j)$ variable, as well as those analogously derived from $p_{\mathrm{T}}(W)$ and $p_{\mathrm{T}}(\gamma)$, are collectively denoted as $\min \Delta\phi(V, j)$. The cuts in $p_{\mathrm{T}}(V)$ and m_{eff} are moderately loosened with respect to the SRs to ensure the data sample size sufficient for the validation. For 2B2Q regions, the J_{bb} mass window cut for the Z_{bb}-/h_{bb}-tagging is loosened to $70 < m_J < 150$ GeV to match CR0L-2B2Q, further increasing the data statistics. The contributions from events containing fake leptons and fake photons are estimated by data-driven methods [135, 136] and are found to be negligible.

The same estimation procedure used to estimate the backgrounds in the SRs is employed to predict the backgrounds in the VRs. A background-only fit, described in Section 9.1, is performed, where the sum of the reducible backgrounds in MC sample is normalized to the data in each CR1L (CR1Y). The modeling of the transfer factor is examined based on the agreement between the data and the post-fit background expectation in the corresponding VR1L (VR1Y). Four sets of fits are performed in the 1L-4Q, 1L-2B2Q, 1Y-4Q and 1Y-2B2Q categories separately. Including all the systematic uncertainties discussed in Section 8, the observed data event yields and the post-fit background expectations in the VRs are summarized in Table 4, and the comparison is visualized in Figure 7. The distributions of m_{eff} in VR1L(1Y)-4Q and m_{T2} in VR1L(1Y)-2B2Q are shown in Figure 8. The data reasonably agree with the estimated backgrounds across the VRs. The largest disagreement is found in VR1L-4Q, corresponding to a statistical significance of 1.8σ.

8 Systematic uncertainties

Uncertainties in the expected signal and background yields account for the statistical uncertainties of the MC samples, the experimental systematic uncertainties associated with the detector measurements and reconstruction, and the theoretical systematic uncertainties on the MC simulation modeling. For the signals and irreducible backgrounds, the uncertainties are assigned directly on the event yields. For the reducible backgrounds, however, they are assigned on the SR(VR)/CR ratio ("transfer factor"; TF) as a consequence of the normalization performed in the CRs. The reducible backgrounds are also subject to the uncertainties due to the limited data statistics in the CRs. Each systematic uncertainty is treated as fully correlated across the analysis regions but not across physics processes, unless explicitly stated otherwise. A summary

Table 3: Summary of selection for the SRs, CRs, and VRs. $n(V_{qq})$ ($n(!V_{qq})$) represents the number of large-R jets passing (failing) the V_{qq}-tagging between the two highest-p_{T} large-R jets. The same selection is applied between the SR (VR) and CR in the same category except for the V_{qq}-tagging and some kinematic selections that are explicitly indicated by the parentheses. The trigger selection and event cleaning described in Section 5 is applied additionally. VRTTX is a validation region for verify the $t\bar{t}+X$ modeling as described in Section 7.1. $p_{\mathrm{T}}(W)$ is the vector sum of the p_{T} of lepton and $E_{\mathrm{T}}^{\mathrm{miss}}$ in the 1L regions. In the 1L (1Y) regions, $E_{\mathrm{T}}^{\mathrm{miss}}$ is replaced by $p_{\mathrm{T}}(W)$ ($p_{\mathrm{T}}(\gamma)$) when calculating the kinematic variables m_{eff}, $\min\Delta\phi(E_{\mathrm{T}}^{\mathrm{miss}}, j)$ and m_{T2}. Details are described in Section 7.2.

	SR(CR0L)		VR(CR)1L		VR(CR)1Y		VRTTX
	4Q	2B2Q	4Q	2B2Q	4Q	2B2Q	
$n_{\text{Large}-R\text{ jets}}$	≥ 2		≥ 2		≥ 2		$= 1$
n_{lepton}	$= 0$		$= 1$		$= 0$		$= 3$
$p_{\mathrm{T}}(\ell_1)$ [GeV]	-		> 30		-		> 30
n_{photon}	-		-		$= 1$		-
$n(V_{qq})$	$= 2\ (= 1)$	$= 1\ (= 0)$	$= 2\ (= 1)$	$= 1\ (= 0)$	$= 2\ (= 1)$	$= 1\ (= 0)$	-
$n(!V_{qq})$	$= 0\ (= 1)$	$= 0\ (= 1)$	$= 0\ (= 1)$	$= 0\ (= 1)$	$= 0\ (= 1)$	$= 0\ (= 1)$	-
$n(J_{bb})$	$= 0$	$= 1$	$= 0$	$= 1$	$= 0$	$= 1$	$= 1$
$m(J_{bb})$ [GeV]	-	$\in [70, 135\ (150)]$	-	$\in [70, 150]$	-	$\in [70, 150]$	-
$n_{b-\text{jet}}^{\text{unmatched}}$	$= 0$		$= 0$		$= 0$		-
$n_{b-\text{jet}}$	≤ 1	-	$= 0$	-	≤ 1	-	-
$E_{\mathrm{T}}^{\mathrm{miss}}$ [GeV]	> 300	> 200	> 50		< 200		-
$p_{\mathrm{T}}(W)$ [GeV]	-		> 200		-		-
$p_{\mathrm{T}}(\gamma)$ [GeV]	-		-		> 200		-
m_{eff} [GeV]	> 1300	$> 1000\ (> 900)$	> 1000	> 900	> 1000	> 900	-
$\min\Delta\phi(E_{\mathrm{T}}^{\mathrm{miss}}, j)$	> 1.0		> 1.0		> 1.0		-
m_{T2} [GeV]	-	> 250	-	> 250	-	> 250	-

of the background prediction uncertainties is shown in Figure 9. The post-fit values are quoted after a "background-only fit" described in Section 9. The MC statistical uncertainties gives the largest contribution to the systematic uncertainty, dominantly from the limited sample statistics of $Z(\rightarrow \nu\nu)$ + jets background used for the extrapolation. However this is not a limiting factor for the analysis sensitivity since the total uncertainty in the SRs are dominated by the statistical uncertainty due to the low data events in the SRs. Details on the experimental and theoretical systematics is described in the following sub-sections.

8.1 Experimental uncertainties

The first class of experimental uncertainties is related to the reconstruction and identification efficiencies for large-R jets, small-R jets, leptons and photons considered in the analysis. These are implemented as uncertainties on the efficiency correction factors applied to the MC, which correct for discrepancies between the efficiency predicted by MC and the efficiency in data, as measured using dedicated control samples.

The uncertainty in W_{qq} (Z_{qq})-tagging provides the dominant contribution to this class of efficiency uncertainties. It originates from the MC modeling uncertainty on the jet substructure variable distributions (m_J, D_2 and n_{trk}), as well as the precision of the efficiency determination in data. The MC modeling uncertainty is evaluated by comparing different MC generator configurations [116]. The data efficiency

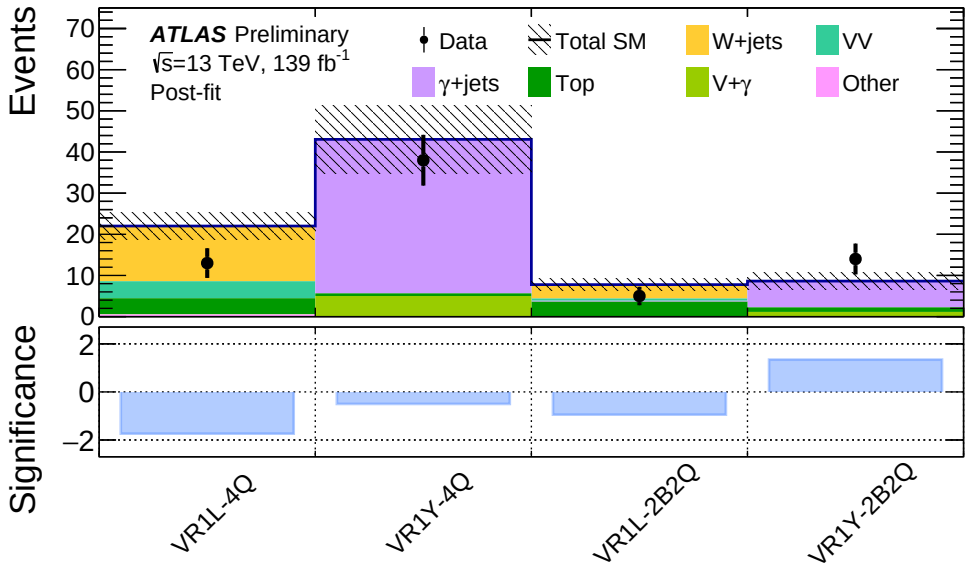

Figure 7: Comparison between the observed data and the post-fit SM background prediction in VR1L and VR1Y. The background predictions are obtained using the background-only fit described in Section 9.1. "Top" includes $t\bar{t}$, $t + X$ and $t\bar{t} + X$ production. The total systematic uncertainty on the background prediction is shown by the hatched band. The bottom panel shows the statistical significance of the discrepancy between the observed number of events and the SM expectation.

is measured for the W_{qq}-tagging using $t\bar{t}$ for signal jets (large-R jets that contain the $W \to qq$ decays) and QCD multi-jet/γ+jets for background jets, following the prescription described in Ref. [116]. The total uncertainty on the W_{qq}-tagging efficiency correction factor ranges from 12% to 23% for signal jets (depending on p_{T}), and about 20% for background jets, respectively. The same efficiency correction factors are applied to the Z_{qq}-tagging selection, with the additional 4–5% uncertainty accounting for the difference between W and Z evaluated based on simulation.

Uncertainty in the Z_{bb} (h_{bb})-tagging is propagated from the b-tagging efficiency uncertainty and the J_{bb} mass shape uncertainty. For the b-tagging uncertainty, 1–10%, 15–50%, and 50–100% uncertainties are assigned on the MC correction factor for b-jets, c-jet mis-tagging, and light-flavour jet mis-tagging, respectively, driven by theoretical uncertainties on the MC efficiency and the data efficiency measurement precision. The J_{bb} mass scale uncertainty is estimated using the R_{trk} method [111], and a relative scale uncertainty of 2–8% is assigned depending on $p_{\mathrm{T},J}$ and m_J. A conservative 20% relative uncertainty is assigned for the J_{bb} mass resolution.

Other efficiency uncertainties related to triggering, identification, reconstruction, and isolation requirements of electrons [60, 119], muons [137] and photons [60], and the jet vertex tagger selection for small-R jets, are found to be negligible.

The second class of experimental uncertainties is related to the energy (or momentum) determination of the reconstructed objects, namely large-R jets [111], small-R jets [123], electrons [119], muons [138] and photons [119]. These are typically from the precision of simulation-based and in-situ calibrations on the energy (momentum) scale and resolution. These per-object uncertainties are propagated through the $E_{\mathrm{T}}^{\mathrm{miss}}$ calculation, with additional uncertainties accounting for the scale and resolution of the soft term [125].

Table 4: Number of observed data events and the post-fit SM background prediction in the VR1L (1Y) bins and the corresponding CR1L (1Y) bins. "-" indicates negligibly small contribution. Note that the relative uncertainty on the expected yield in the CRs between the reducible backgrounds are identical, given that a common normalization factor is assigned for all of them in the fit.

Region	CR1L-4Q	VR1L-4Q	CR1L-2B2Q	VR1L-2B2Q
Observed	439	13	96	5
Post-fit	439 ± 21	22.0 ± 3.4	96 ± 10	7.8 ± 1.5
W + jets	325 ± 16	13.4 ± 2.2	48 ± 5	3.4 ± 0.7
Z + jets	4.45 ± 0.21	0.198 ± 0.035	0.58 ± 0.06	0.044 ± 0.012
γ + jets	< 1	-	0.57 ± 0.06	0.22 ± 0.10
VV	65.4 ± 3.1	4.1 ± 0.8	6.9 ± 0.7	0.55 ± 0.15
$V\gamma$	< 1	-	< 0.1	-
VVV	1.3 ± 0.6	0.52 ± 0.28	0.14 ± 0.08	0.09 ± 0.05
$t\bar{t}$	30.4 ± 1.5	2.7 ± 0.4	24.0 ± 2.5	1.8 ± 0.4
$t + X$	11.0 ± 0.5	0.91 ± 0.21	13.2 ± 1.4	1.27 ± 0.34
$t\bar{t} + X$	1.5 ± 1.2	0.16 ± 0.12	1.5 ± 1.1	0.4 ± 0.4
Vh	< 0.1	< 0.001	0.69 ± 0.07	0.046 ± 0.009
Region	CR1Y-4Q	VR1Y-4Q	CR1Y-2B2Q	VR1Y-2B2Q
Observed	1001	38	127	14
Post-fit	1001 ± 32	43 ± 8	127 ± 11	8.6 ± 2.0
W + jets	2.59 ± 0.08	< 0.1	< 0.1	-
Z + jets	< 1	-	< 0.01	-
γ + jets	856 ± 28	37 ± 7	107 ± 11	6.4 ± 1.6
VV	< 1	-	-	-
$V\gamma$	131 ± 4	5.0 ± 0.9	12.6 ± 1.3	1.13 ± 0.27
VVV	< 0.1	< 0.01	-	-
$t\bar{t}$	1.28 ± 0.04	-	0.57 ± 0.06	0.28 ± 0.18
$t + X$	< 1	-	< 0.1	-
$t\bar{t} + X$	9 ± 6	0.6 ± 0.5	7 ± 5	0.8 ± 0.6
Vh	< 0.001	-	< 0.01	-

Additionally, an uncertainty is considered on the integrated luminosity used for normalizing the MC samples. A 1.7% uncertainty is quoted for the combined 2015–2018 integrated luminosity obtained primarily using the LUCID-2 detector [139]. Finally, the pile-up modeling uncertainty is assigned based on the discrepancy in the predicted and measured inelastic cross-sections [140].

8.2 Theoretical uncertainties

Theoretical uncertainties on the main reducible backgrounds W/Z+jets, γ+jets and VV production are estimated with varied generator parameters. Uncertainties due to the choice of QCD renormalization and factorization scales are evaluated by varying them up and down by a factor of two with respect to the nominal values [141]. For W/Z+jets, the uncertainties related to the choice of CKKW merging scale is also considered. These are assessed by shifting the merging scale to 15 GeV or 30 GeV from the default scale of 20 GeV. For the $t\bar{t}$ background, the nominal POWHEG+PYTHIA8 sample is compared to an alternative sample generated using MG5_aMC@NLO for evaluating the hard scattering modeling uncertainty; and to a

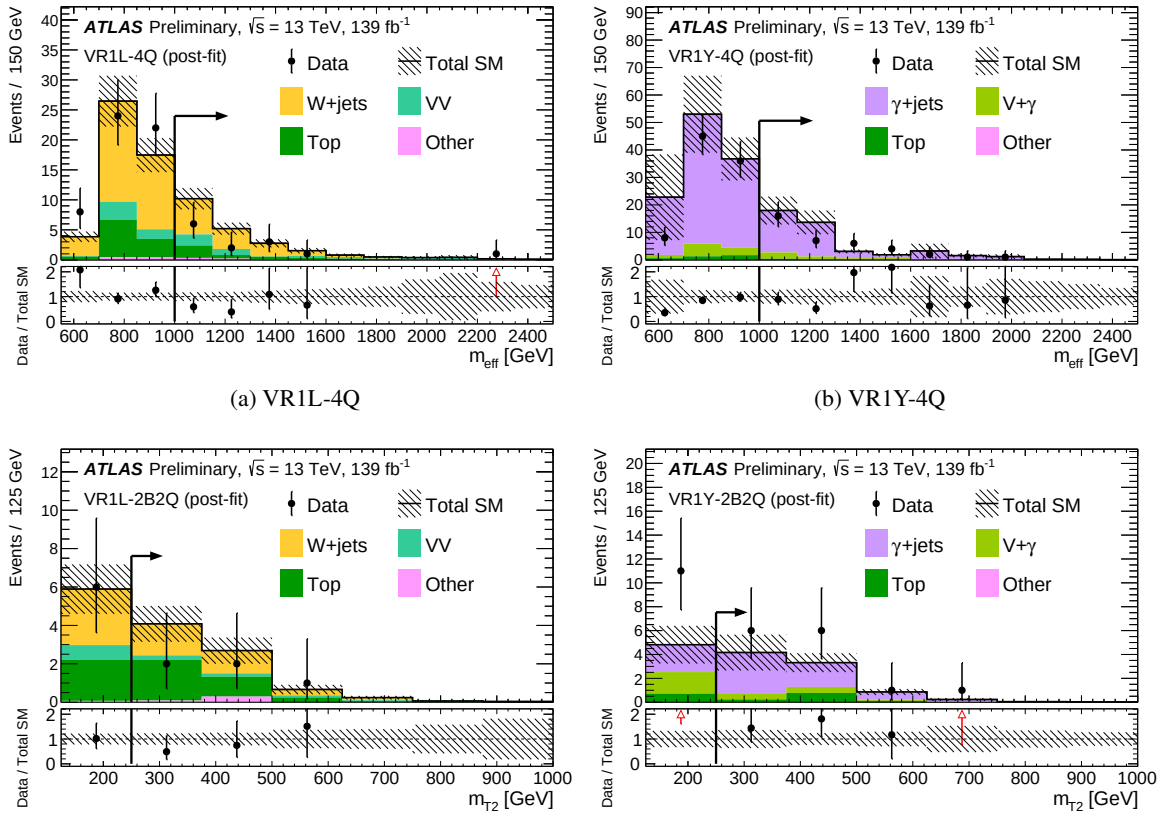

(a) VR1L-4Q

(b) VR1Y-4Q

(c) VR1L-2B2Q

(d) VR1Y-2B2Q

Figure 8: m_{eff} distributions in VR1L-4Q/VR1Y-4Q and m_{T2} distributions in VR1L-2B2Q/VR1Y-2B2Q. The post-fit SM background expectation using the background-only fit is shown in a histogram stack. "Top" includes $t\bar{t}$, $t+X$ and $t\bar{t}+X$ production. The hatched bands indicate the combined statistical and systematic uncertainty on the background. The bottom panels show the ratio of the observed data to the background expectation. The selection criterion on the variable shown by each plot is removed, while the arrow indicates the cut value to define the region.

sample generated using POWHEG interfaced to HERWIG 7.0.4 [142] and H7UE set of tuned parameters [142] for assessing the uncertainty on the choice of parton shower scheme and hadronisation model. Variations in the $t\bar{t}$ initial- and final-state radiation modeling, renormalisation and factorisation scales are also considered following the prescription described in Ref. [143]. Uncertainties related to the choice of NNPDF30NNLO PDF sets are assigned for the W/Z+jets, γ+jets, VV, $t\bar{t}$ and single-top backgrounds. These are derived by taking the envelope of the eigenvector variation out of 100 propagated uncertainties.

For the reducible background estimation, an additional uncertainty is assigned for the modeling of the relative background composition. This is to account for that different physics processes ($Z+$jets, $W+$jets, $t\bar{t}\ldots$) are considered altogether in the fits, and therefore the composition is solely predicted by the simulation. While the estimation is insensitive to the composition at the first order since the TFs of those physics processes are similar, the residual TF difference can cause a bias in the estimation when the composition is significantly mis-modeled by the simulation. The impact of the potential composition mis-modeling is evaluated by the variation in the combined TF when shifting the normalization of each physics process up and down by a factor of two. An uncertainty of about 2–8% is assigned in the 4Q category, while 7–10% is assigned for those in the 2B2Q category.

For the irreducible backgrounds, cross-section uncertainties are assigned to account for their normalization. A 50% uncertainty is used for VVV production, while a 70% normalization uncertainty is assigned for $t\bar{t} + X$ based on the data/MC discrepancy observed in VRTTX, as discussed in Section 7.1.

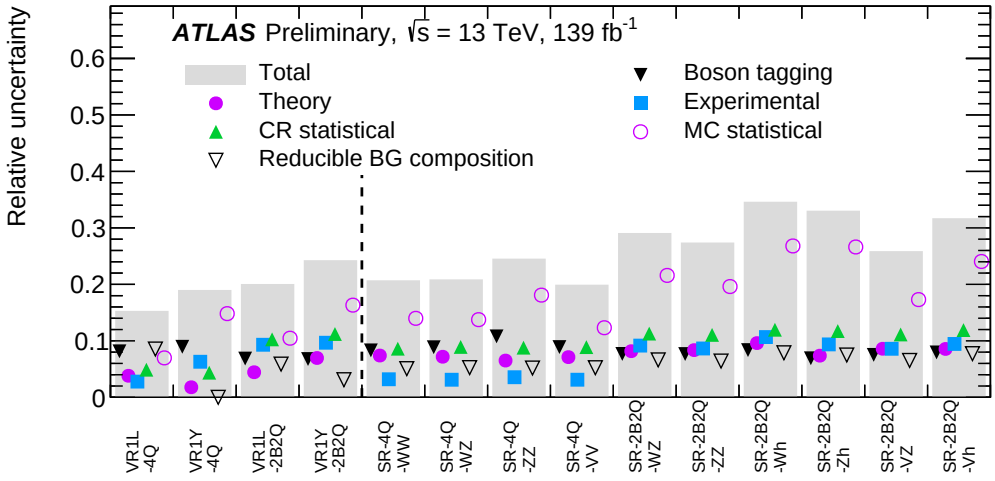

Figure 9: The total post-fit uncertainty and the breakdown in each of the SRs and VRs. "MC statistical" and "CR statistical" present the statistical uncertainty due to the limited sample size either in the MC (dominantly due to the $Z(\rightarrow \nu\nu)$ + jets sample size) or in the CR data, respectively. "Boson tagging" indicates the uncertainty on the W_{qq} (Z_{qq})-tagging efficiency, while "experimental" shows the contribution from the rest of the experimental uncertainties. "Reducible BG composition" refers to the uncertainty in the reducible background estimation due to the relative composition uncertainty. "Theory" represents the total uncertainty from all the theoretical uncertainties.

Uncertainty on the signal yields consists of the cross-section uncertainty and the shape uncertainties. The cross-section uncertainty ranges from 6-20% for the production of electroweakinos with masses between 400 GeV and 1 TeV, mainly driven by the PDF uncertainty. The shape uncertainties comprise uncertainties in the choice of renormalization/factorization scales and parton shower modeling, affecting the signal acceptance by 5–10%.

9 Results

9.1 Statistical Analysis

Final background estimates are obtained by performing a profile log-likelihood fit [144, 145] simultaneously in all CRs and SRs relevant to a given interpretation. The HistFitter [146] framework is employed. Systematic uncertainties are treated as Gaussian distributed nuisance parameters in the likelihood, while the statistical uncertainties of the MC samples are treated as Poisson distributed nuisance parameters.

Three types of fit configurations are used to derive the results.

- A "*background-only fit*" is performed considering only the CRs and assuming no contribution from signals. The normalization of the total reducible backgrounds is allowed to float and is constrained by the fit using the data in the CRs. The normalization factors and nuisance parameters are adjusted by maximizing the likelihood. Three independent sets of fit are performed in the 0L, 1L, and 1Y categories, respectively. The 4Q and 2B2Q regions in each category are fitted simultaneously,

however with independent normalization factors assigned in 4Q and 2B2Q. The normalization factors obtained from the fits range from 0.7 to 1.3.

- A "*discovery fit*" performs the hypothesis test for a generic beyond-the-SM (BSM) signal, setting upper limits on the number of events and visible cross-section for the signal. The fit uses only a single SR and the associated CR0L bin(s), constraining the backgrounds following the same method as in the background-only fit. Any contribution from signal is only allowed only in the SR, and the signal-strength parameter is defined to be strictly positive.
- An "*exclusion fit*" is performed to set the exclusion limit for a given signal model. The SRs and the corresponding CR0L bins are fit simultaneously to determine the reducible background normalization factors and constrain the systematics. The signal contamination in CR0L is also taken into account according to the model predictions.

For each discovery or exclusion fit, the compatibility of the observed data with the background-only or signal-plus-background hypotheses is expressed by the CL_s metric [147]. The 95% confidence level (CL) exclusion is defined by $CL_s < 0.05$.

Table 5: Number of observed data events and the SM backgrounds in the SRs and the CR0L bins. The SM backgrounds are predicted by the background-only fits. "-" indicates negligible contribution. Note that the relative uncertainty on the expected yield in the CRs between the reducible backgrounds are identical, given that a common normalization factor is assigned for all of them in the fit.

Region	CR0L-4Q	CR0L-2B2Q	SR-4Q-WW	SR-4Q-WZ	SR-4Q-ZZ	SR-4Q-VV
Observed	129	83	2	3	1	3
Post-fit	129 ± 11	83 ± 9	1.9 ± 0.4	3.4 ± 0.7	1.9 ± 0.5	3.9 ± 0.8
W+jets	24.2 ± 2.2	16.6 ± 2.0	0.37 ± 0.08	0.60 ± 0.13	0.26 ± 0.07	0.69 ± 0.15
Z+jets	78 ± 7	44 ± 5	1.0 ± 0.21	1.8 ± 0.4	1.26 ± 0.32	2.1 ± 0.4
VV	21.5 ± 1.9	7.1 ± 0.9	0.35 ± 0.11	0.73 ± 0.24	0.26 ± 0.09	0.79 ± 0.25
VVV	0.9 ± 0.4	0.10 ± 0.05	0.17 ± 0.09	0.19 ± 0.10	0.11 ± 0.07	0.23 ± 0.12
$t\bar{t}$	1.38 ± 0.12	7.8 ± 0.9	0.039 ± 0.009	0.060 ± 0.018	0.025 ± 0.010	0.063 ± 0.018
$t + X$	1.32 ± 0.12	2.87 ± 0.34	0.015 ± 0.006	0.039 ± 0.016	0.012 ± 0.005	0.039 ± 0.016
$t\bar{t} + X$	1.3 ± 0.9	3.7 ± 2.6	-	-	-	-
Other	< 0.1	0.95 ± 0.11	< 0.001	< 0.001	< 0.001	< 0.001

Region	SR-2B2Q-WZ	SR-2B2Q-Wh	SR-2B2Q-ZZ	SR-2B2Q-Zh	SR-2B2Q-VZ	SR-2B2Q-Vh
Observed	2	0	2	1	2	1
Post-fit	1.6 ± 0.4	1.9 ± 0.7	1.7 ± 0.5	1.6 ± 0.5	2.2 ± 0.6	2.5 ± 0.8
W+jets	0.11 ± 0.06	0.24 ± 0.09	0.23 ± 0.08	0.26 ± 0.10	0.26 ± 0.09	0.26 ± 0.09
Z+jets	0.84 ± 0.27	1.3 ± 0.5	0.78 ± 0.23	0.66 ± 0.24	1.15 ± 0.33	1.4 ± 0.5
VV	0.33 ± 0.11	0.09 ± 0.03	0.32 ± 0.10	0.085 ± 0.032	0.37 ± 0.11	0.085 ± 0.030
VVV	0.047 ± 0.027	< 0.01	0.051 ± 0.032	0.011 ± 0.007	0.06 ± 0.04	0.011 ± 0.007
$t\bar{t}$	0.016 ± 0.006	0.13 ± 0.04	0.064 ± 0.019	0.40 ± 0.16	0.072 ± 0.021	0.46 ± 0.18
$t + X$	0.11 ± 0.05	0.07 ± 0.04	0.11 ± 0.05	0.041 ± 0.022	0.11 ± 0.05	0.10 ± 0.05
$t\bar{t} + X$	0.10 ± 0.08	$0.07^{+0.10}_{-0.07}$	0.14 ± 0.12	$0.08^{+0.09}_{-0.08}$	0.18 ± 0.14	$0.10^{+0.11}_{-0.10}$
Other	< 0.01	0.03 ± 0.01	< 0.01	0.024 ± 0.008	< 0.01	0.037 ± 0.011

9.2 Signal region yields

The observed data yields in each SR and CR0L together with their SM background expectations are summarized in Tables 5 and visualized in Figure 10. No significant excess is found in any of the SRs. The distributions of m_{eff} in SR-4Q-VV and m_{T2} in SR-2B2Q-VZ and SR-2B2Q-Vh are shown in Figure 11 with some representative signal samples overlaid to illustrate the sensitivity.

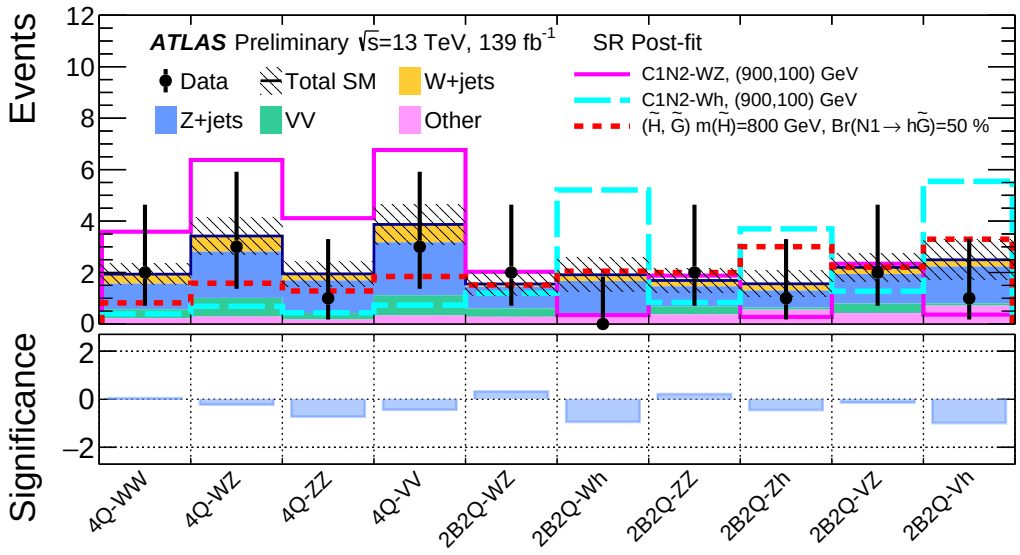

Figure 10: Summary of the observed data and predicted SM background in all SRs. The background prediction in SR-4Q (SR-2B2Q) is obtained by a background-only fit to CR0L-4Q (CR0L-2B2Q). The total systematic uncertainty on the background prediction is shown by the hatched area. Distributions of a few representative signals are overlaid. A few representative signals are overlaid. For the $(\widetilde{W},\widetilde{B})$-SIM models, the label (x, y) indicates $(m(\widetilde{\chi}_1^{\pm}), m(\widetilde{\chi}_1^0)) = (x, y)$ GeV. The bottom panel shows the statistical significance of the discrepancy between the observed number of events and the SM expectation.

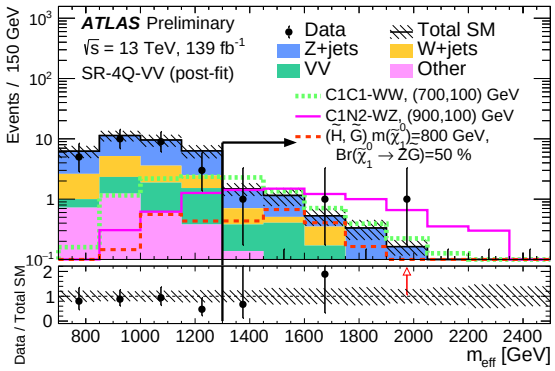

(a) SR-4Q-VV

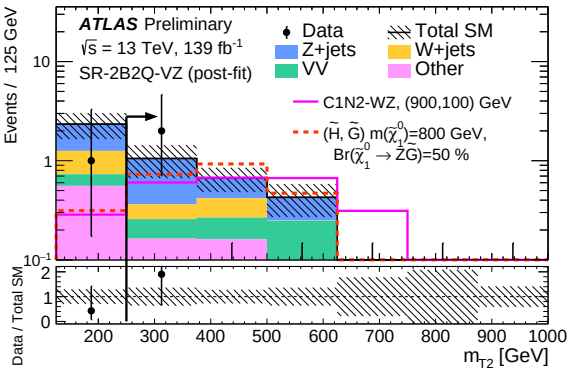

(b) SR-2B2Q-VZ

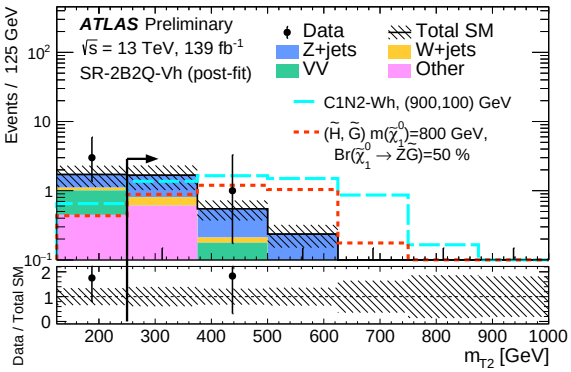

(c) SR-2B2Q-Vh

Figure 11: (a) m_{eff} distribution in SR-4Q-VV. (b)-(c) m_{T2} distributions in SR-2B2Q-VZ and SR-2B2Q-Vh. The post-fit SM background expectation using the background-only fit is shown in a histogram stack. Distributions of a few representative signals are overlaid. The bottom panels show the ratio of the observed data to the background prediction. The selection criteria on the variable shown by each plot is removed, while the arrow indicates the cut value to define the region. A few representative signals are overlaid. For the $(\widetilde{W}, \widetilde{B})$-SIM models, the label (x, y) indicates $(m(\widetilde{\chi}_1^{\pm}), m(\widetilde{\chi}_1^0)) = (x, y)$ GeV.

Table 6: Left to right: 95% CL upper limits on the visible cross section ($\langle\epsilon\sigma\rangle^{95}_{obs}$). S^{95}_{obs} (S^{95}_{exp}) shows the 95% CL upper limit on the number of signal events, given the observed number (expected number and $\pm1\sigma$ excursions) of background events. The last two columns indicate the CL_B value and the discovery p-value ($p(s) = 0$) with the corresponding gaussian significance (Z). CL_B provides a measure of the disagreement of the observation with the background-only hypothesis by quantifying how frequently a measurement suggesting a higher signal contribution than the best fit signal strength would occur due to background fluctuations, whilst the p_0 value instead quantifies the excess of data given the null hypothesis of background only. By convention, the quoted p-value is truncated at 0.5 in the case of a data deficit.

Signal region	$\langle\epsilon\sigma\rangle^{95}_{obs}$[fb]	S^{95}_{obs}	S^{95}_{exp} ($\pm1\sigma$)	CL_B	$p(s = 0)$ (Z)
SR-4Q-WW	0.032	4.5	$4.2^{+1.8}_{-1.0}$	0.55	0.44 (0.15)
SR-4Q-WZ	0.036	5.0	$5.1^{+2.1}_{-1.3}$	0.46	0.50 (0.00)
SR-4Q-ZZ	0.025	3.6	$4.1^{+1.8}_{-1.0}$	0.30	0.50 (0.00)
SR-4Q-VV	0.034	4.7	$5.3^{+2.3}_{-1.5}$	0.38	0.50 (0.00)
SR-2B2Q-WZ	0.033	4.7	$4.0^{+1.7}_{-0.7}$	0.66	0.33 (0.44)
SR-2B2Q-Wh	0.022	3.1	$3.9^{+1.3}_{-0.7}$	0.28	0.50 (0.00)
SR-2B2Q-ZZ	0.033	4.5	$4.1^{+1.7}_{-0.9}$	0.63	0.37 (0.32)
SR-2B2Q-Zh	0.026	3.6	$3.9^{+1.4}_{-0.7}$	0.38	0.50 (0.00)
SR-2B2Q-VZ	0.032	4.4	$4.4^{+1.8}_{-1.0}$	0.50	0.50 (0.00)
SR-2B2Q-Vh	0.026	3.6	$4.4^{+1.7}_{-1.0}$	0.24	0.50 (0.00)
Disc-SR-2B2Q	0.034	4.8	$5.6^{+2.4}_{-1.6}$	0.30	0.50 (0.00)
Disc-SR-Incl	0.042	5.9	$7.2^{+2.2}_{-2.0}$	0.27	0.50 (0.00)

9.3 Model-independent upper limits

The model-independent fit is performed for each SR to derive the expected and observed 95% CL upper limits on the number of BSM signal events (S^{95}_{exp} and S^{95}_{obs}) as well as the one-sided p-value (p_0) of the background-only hypothesis. S^{95}_{obs} is also converted to the upper limit on the cross-section, $\langle\epsilon\sigma\rangle^{95}_{\text{obs}}$ where ϵ represents the efficiency times acceptance of the SR to the given signal, by dividing by the integrated luminosity. The upper limits and the p_0 value associated with each SR are summarized in Table. 6. Two additional SR regions are defined to set the upper limits in the inclusive phase space; two "discovery SRs" are defined that are only used for deriving the model-independent upper limits; Disc-SR-2B2Q is defined as the logical union of SR-2B2Q-VZ and SR-2B2Q-Vh; and Disc-SR-Incl is defined as the logical union of SR-4Q-VV and Disc-SR-2B2Q. Both CR0L-4Q and CR0L-2B2Q join the simultaneous fit with two independent normalization factors assigned for the reducible backgrounds when evaluating Disc-SR-Incl.

9.4 Model-dependent exclusion limits

The results are also interpreted in the context of the specific signal models discussed in Section 2. A model-dependent fit and a hypothesis test is performed for each point in the model space. The expected and observed 95% CL exclusion are derived based on a threshold of $\mathrm{CL_s} < 0.05$.

The SRs participating the simultaneous fit vary by the signal models being tested, which is summarized in Table 1. CR0L-4Q (CR0L-2B2Q) is included in the fit when at least one SR-4Q (SR-2B2Q) bin is used for deriving the limit, while both of the CR0L bins are included when the SR bins from both SR-4Q and SR-2B2Q participate in the fit.

9.4.1 Exclusion Limit on $(\widetilde{W},\widetilde{B})$, $(\widetilde{H},\widetilde{B})$, $(\widetilde{W},\widetilde{H})$, and $(\widetilde{H},\widetilde{W})$ models

The exclusion limits on the $(\widetilde{W},\widetilde{B})$ and $(\widetilde{H},\widetilde{B})$ models are summarized in Figure 12. As discussed in Section 2.1, different $\mathcal{B}(\widetilde{\chi}_2^0 \to Z\widetilde{\chi}_1^0)$ hypotheses are examined, which are shown to result in highly similar limits in Figure 12(a) and 12(b).

The expected and observed limits for a representative slice $\mathcal{B}(\widetilde{\chi}_2^0 \to Z\widetilde{\chi}_1^0) = 50\%$ are shown in Figure 12(c) and 12(d), for $(\widetilde{W},\widetilde{B})$ and $(\widetilde{H},\widetilde{B})$ models respectively.

The exclusion limits set on the $(\widetilde{W},\widetilde{H})$ and $(\widetilde{H},\widetilde{W})$ models are evaluated in a three-dimensional model space defined by $(M_2,\mu,\tan\beta)$. For each model point, the mass spectra and the branching ratios are determined using the prescription described in Section 2.1. Figure 13(a) shows the expected and the observed limit presented as a function of (M_2,μ) with a fixed $\tan\beta = 10$. Figure 13(b) shows the effect of varying $\tan\beta$, where very little dependency on $\tan\beta$ and the sign of μ ($\mathrm{sign}(\mu)$) is found for the sensitivity. The limits are also interpreted as a function of the physical electroweakino masses so that they can be directly compared with the other models. For a given set of $(\tan\beta, \mathrm{sign}(\mu))$, a pair of $(M_2, |\mu|)$ can be projected one-to-one to $(m(\widetilde{\chi}_2^\pm), m(\widetilde{\chi}_1^0))$ when all the other MSSM parameters are fixed. Figure 13(c) and Figure 13(d) show the limits for the $(\widetilde{W},\widetilde{H})$ model ($M_2 > |\mu|$) and $(\widetilde{H},\widetilde{W})$ model ($M_2 < |\mu|$), respectively, assuming $\tan\beta = 10$ and $\mu > 0$.

The mass exclusion limits are shown to be highly stable with respect to the internal variations within each model. The limits between $(\widetilde{W},\widetilde{B})$ and $(\widetilde{W},\widetilde{H})$ (or $(\widetilde{H},\widetilde{B})$ and $(\widetilde{H},\widetilde{W})$) are also very similar, despite the branching ratios of $\widetilde{\chi}_{\mathrm{heavy}}$ that are substantially different between the models. This model dependency is small mostly due to the statistical combination of SR-4Q and SR-2B2Q, and the inclusive SR bins (SR-4Q-VV, SR-2B2Q-VZ, and SR-2B2Q-Vh), which are designed to be agnostic to the difference between W- and Z-bosons.

To summarize, a wino mass between 400 GeV and 1060 GeV is excluded for the wino production models for $m(\widetilde{\chi}_1^0) < 400$ GeV; and a higgsino mass between 450 GeV and 900 GeV is excluded for the higgsino production models for $m(\widetilde{\chi}_1^0) < 240$ GeV.

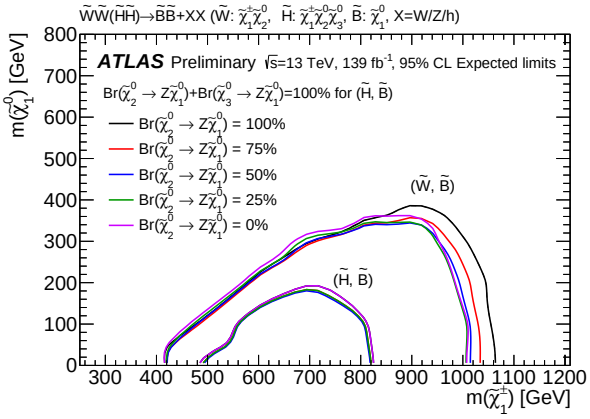

(a) Expected limits with various $\mathcal{B}(\widetilde{\chi}_2^0 \to Z\widetilde{\chi}_1^0)$

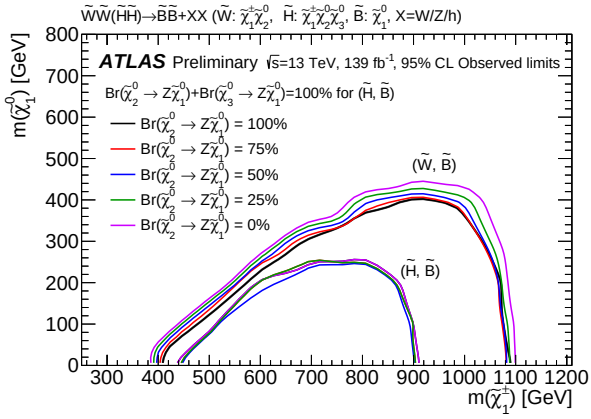

(b) Observed limits with various $\mathcal{B}(\widetilde{\chi}_2^0 \to Z\widetilde{\chi}_1^0)$

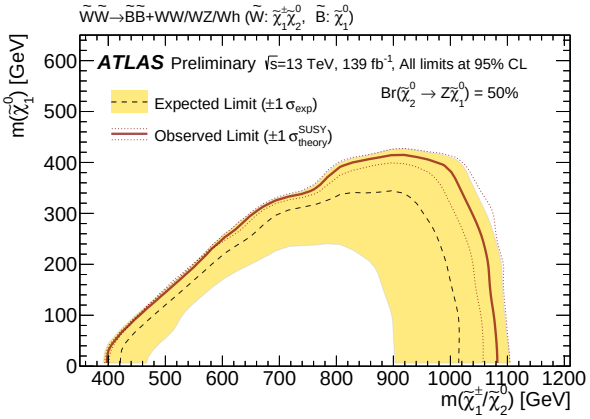

(c) $(\widetilde{W}, \widetilde{B})$ with $\mathcal{B}(\widetilde{\chi}_2^0 \to Z\widetilde{\chi}_1^0) = 50\%$

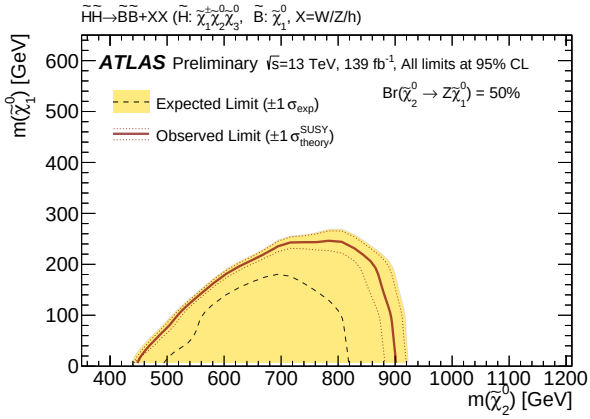

(d) $(\widetilde{H}, \widetilde{B})$ with $\mathcal{B}(\widetilde{\chi}_2^0 \to Z\widetilde{\chi}_1^0) = 50\%$

Figure 12: Exclusion limits for the $(\widetilde{W}, \widetilde{B})$ and $(\widetilde{H}, \widetilde{B})$ models shown as a function of the mass of wino/higgsino chargino ($m(\widetilde{\chi}_1^\pm)$) and the mass of bino LSP ($m(\widetilde{\chi}_1^0)$). (a)-(b) Expected and observed limits for various $\mathcal{B}(\widetilde{\chi}_2^0 \to Z\widetilde{\chi}_1^0)$ hypotheses overlaid. The outer and inner bundles correspond to the limits for the $(\widetilde{W}, \widetilde{B})$ and $(\widetilde{H}, \widetilde{B})$ models respectively. (c)-(d) Expected (dashed) and observed (solid red) 95% CL exclusion limits for a representative branching ratio $\mathcal{B}(\widetilde{\chi}_2^0 \to Z\widetilde{\chi}_1^0) = 50\%$.

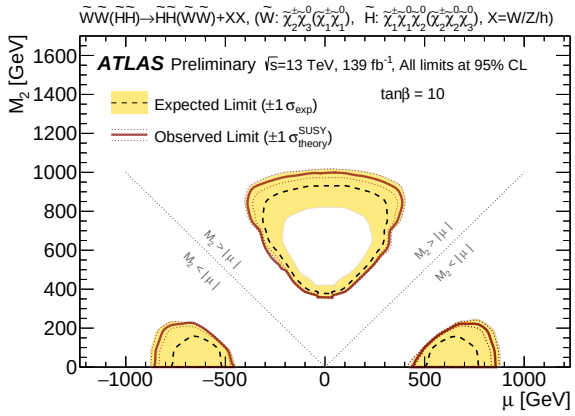

(a) Limits vs (M_2, μ) with $\tan\beta = 10$

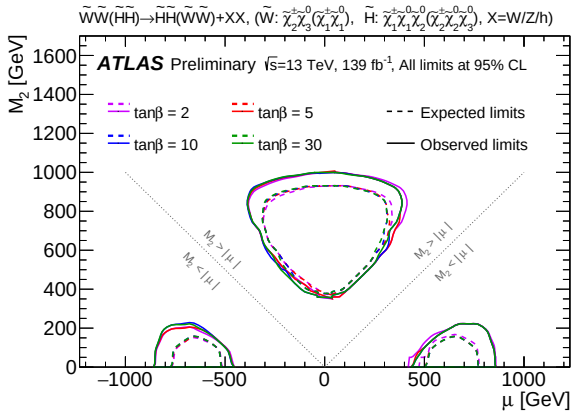

(b) Limits vs (M_2, μ) with varying $\tan\beta$

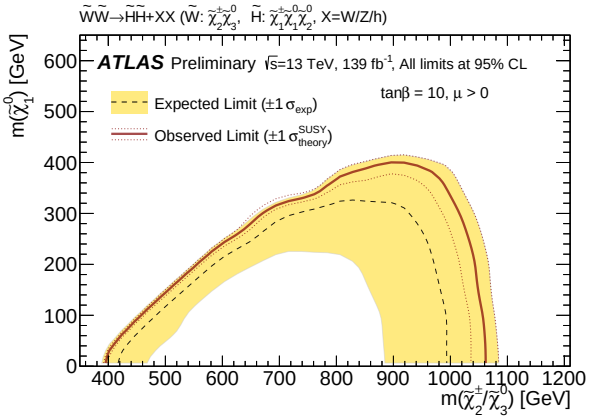

(c) $(\widetilde{W}, \widetilde{H})$ with $\tan\beta = 10, \mu > 0$

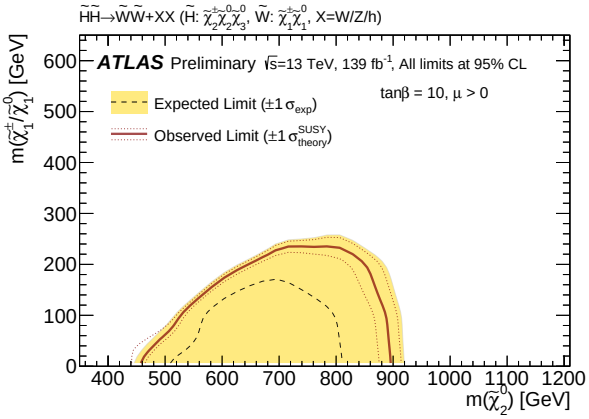

(d) $(\widetilde{H}, \widetilde{W})$ with $\tan\beta = 10, \mu > 0$

Figure 13: 95% CL exclusion limits for the $(\widetilde{W}, \widetilde{H})$ and $(\widetilde{H}, \widetilde{W})$ models. The limits are projected on to a two-dimensional plane either as a function of the wino/higgsino mass parameters: (M_2, μ) (top figures), or of the physical electroweakino masses $(m(\widetilde{\chi}_2^{\pm}), m(\widetilde{\chi}_1^0))$ representing $(m(\widetilde{\chi}_{\text{heavy}}), m(\widetilde{\chi}_{\text{light}}))$ (bottom figures). For the limits shown on the (M_2, μ) plane, the excluded regions are indicated by the area inside the contours. The round excluded area on the top part corresponds to the excluded parameter space in the $(\widetilde{W}, \widetilde{H})$ model $(M_2 > |\mu|)$, while the two small areas at the bottom are that in the $(\widetilde{H}, \widetilde{W})$ model $(M_2 < |\mu|)$.

9.4.2 Exclusion Limit on $(\widetilde{W}, \widetilde{B})$ simplified model: $(\widetilde{W}, \widetilde{B})$-SIM

The exclusion limits for the $(\widetilde{W}, \widetilde{B})$ simplified models (C1C1-WW, C1N2-WZ and C1N2-Wh) are also derived, in order to directly compare the search sensitivity with the previous ATLAS analyses. Figure 14 shows the obtained exclusion as a function of the produced wino mass ($m(\widetilde{\chi}_1^{\pm}/\widetilde{\chi}_2^0)$) and the bino LSP mass ($m(\widetilde{\chi}_1^0)$). For C1C1-WW, $m(\widetilde{\chi}_1^{\pm})$ between 630 GeV and 760 GeV is excluded for $m(\widetilde{\chi}_1^0) < 80$ GeV. For C1N2-WZ (C1N2-Wh), $m(\widetilde{\chi}_1^{\pm}/\widetilde{\chi}_2^0)$ between 440 GeV and 960 GeV (400 GeVand 1060 GeV) is excluded for $m(\widetilde{\chi}_1^0) < 300$ GeV (420 GeV).[13]

The sensitivity to high mass winos is significantly extended with respect to ATLAS searches using the other final states and the same dataset. For example, the expected limits on C1N2-WZ (C1N2-Wh) are typically extended by about 300 (140) GeV in $m(\widetilde{\chi}_1^{\pm}/\widetilde{\chi}_2^0)$, corresponding to exclusion of signals with 7.5 (2.4) smaller production cross-section, with respect to the search using final states with three leptons [19, 20] (one lepton and two b-jets [24]). This result also sets the most stringent limit on the model to date across the LHC experiments.

9.4.3 Exclusion Limits on $(\widetilde{H}, \widetilde{G})$ model

The exclusion for the $(\widetilde{H}, \widetilde{G})$ model is presented in Figure 15, as the function of mass of the lightest higgsino ($m(\widetilde{\chi}_1^0)$) and the branching ratio $\mathcal{B}(\widetilde{\chi}_1^0 \to Z\widetilde{G})$. For $\mathcal{B}(\widetilde{\chi}_1^0 \to Z\widetilde{G}) = 100\ (50)\%$, $m(\widetilde{\chi}_1^0)$ between 450 (500) GeV and 940 (850) GeV is excluded, while the exclusion reaches $\mathcal{B}(\widetilde{\chi}_1^0 \to Z\widetilde{G}) \sim 20\%$ for $m(\widetilde{\chi}_1^0) \sim 600$ GeV. This complements the sensitivity achieved by previous ATLAS searches using 4-lepton final states to target signals decaying into ZZ [26] and final states with three or more b-jets to target signals decaying into hh [25].

9.4.4 Exclusion Limits on $(\widetilde{H}, \tilde{a})$ model

Lastly, Figure 16 shows the exclusion limits on the $(\widetilde{H}, \tilde{a})$ model as the function of axino mass ($m(\tilde{a})$) and the lightest higgsino ($m(\widetilde{\chi}_1^0)$). Similar to the $(\widetilde{H}, \widetilde{G})$ model, different branching ratio hypotheses of $\mathcal{B}(\widetilde{\chi}_1^0 \to Z\tilde{a})(= 1 - \mathcal{B}(\widetilde{\chi}_1^0 \to h\tilde{a}))$ are tested. For $\mathcal{B}(\widetilde{\chi}_1^0 \to Z\tilde{a}) = 100\%$, a higgsino mass between 450 GeV and 940 GeV is excluded when the axino mass is less than 300 GeV. The sensitivity decreases with decreasing $\mathcal{B}(\widetilde{\chi}_1^0 \to Z\tilde{a})$. For $\mathcal{B}(\widetilde{\chi}_1^0 \to Z\tilde{a}) = 50\%$, the observed limit excludes higgsino masses between 500 − 850 GeV when the axino mass is less than 210 GeV.

[13] The obtained limits are generally weaker than that set to the $(\widetilde{W}, \widetilde{B})$ model shown in Section 9.4.1. This is because only one production mode is considered in these simplified models, while multiple production modes are included in the signals in the $(\widetilde{W}, \widetilde{B})$ model.

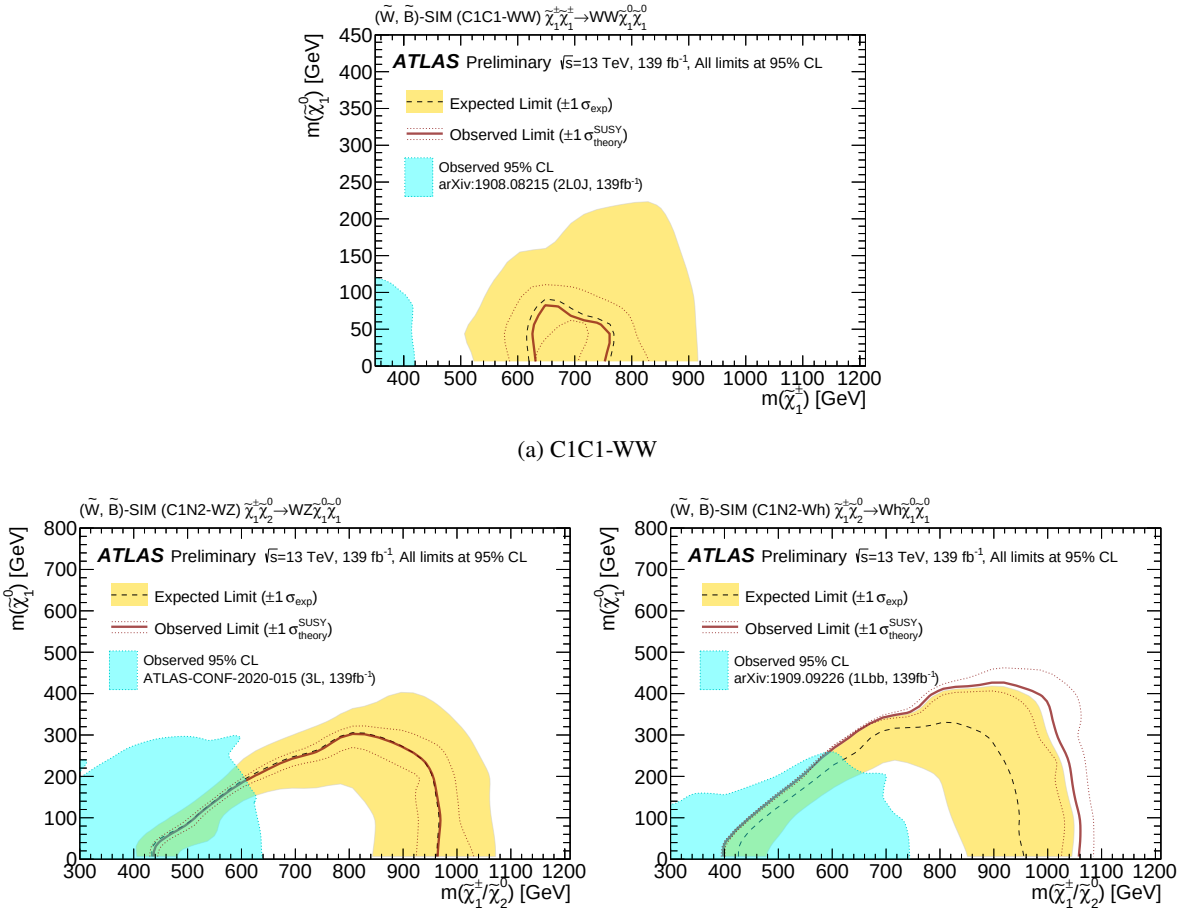

(a) C1C1-WW

(b) C1N2-WZ

(c) C1N2-Wh

Figure 14: Exclusion limits for $(\widetilde{W}, \widetilde{B})$-SIM as a function of the produced wino mass ($m(\widetilde{\chi}_1^{\pm}/\widetilde{\chi}_2^0)$) and the bino LSP mass ($m(\widetilde{\chi}_1^0)$). Expected (dashed) and observed (solid) 95% CL exclusion limits on $(\widetilde{W}, \widetilde{B})$ simplified models; (a) C1C1-WW, (b) C1N2-WZ, and (c) C1N2-Wh. The limits from the previous ATLAS searches on C1C1-WW [18], C1N2-WZ [19], and C1N2-Wh [24] are shown by the shaded areas.

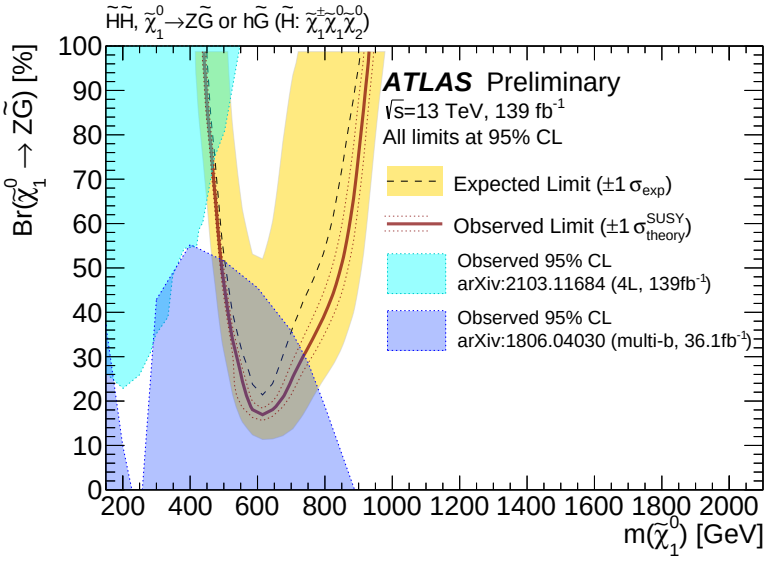

Figure 15: Expected (dashed) and observed (solid red) 95% CL exclusion limit derived for the $(\widetilde{H}, \widetilde{G})$ model, as a function of the lightest higgsino mass ($m(\widetilde{\chi}_1^0)$) and the branching ratio $\mathcal{B}(\widetilde{\chi}_1^0 \to Z\widetilde{G})(= 1 - \mathcal{B}(\widetilde{\chi}_1^0 \to h\widetilde{G}))$. The excluded region is indicated by the area inside the contour. The exclusion limits from the previous ATLAS search using 4-lepton final states [26] (cyan, denoted as "4L"), or final states with three or more b-jets [25] (violet, denoted as "multi-b") are shown by the shaded areas.

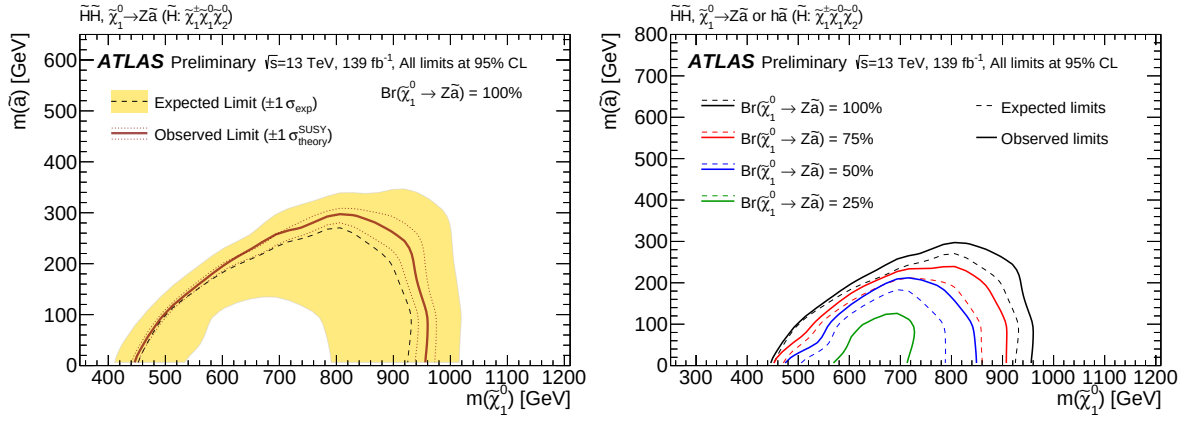

(a) $\mathcal{B}(\widetilde{\chi}_1^0 \to Z\tilde{a}) = 100\%$ (b) Variable $\mathcal{B}(\widetilde{\chi}_1^0 \to Z\tilde{a})$

Figure 16: 95% CL exclusion limits for the $(\widetilde{H}, \tilde{a})$ model as the function of axino mass ($m(\tilde{a})$) and the lightest higgsino ($m(\widetilde{\chi}_1^0)$). (a) Expected (dashed line) and observed (solid red line) limits calculated for $\mathcal{B}(\widetilde{\chi}_1^0 \to Z\tilde{a}) = 100\%$. (b) Expected (dashed lines) and observed (solid lines) limits with various $\mathcal{B}(\widetilde{\chi}_1^0 \to Z\tilde{a})(= 1 - \mathcal{B}(\widetilde{\chi}_1^0 \to h\tilde{a}))$ hypotheses. No expected limit is derived for the case with $\mathcal{B}(\widetilde{\chi}_1^0 \to Z\tilde{a}) = 25\%$ as no mass point on the plane can be excluded.

10 Conclusion

A search for electroweakino pair production using final states consisting of $E_{\mathrm{T}}^{\mathrm{miss}}$ and two boosted hadronically-decaying heavy SM bosons (W, Z, or h) is reported. Signatures with large mass splitting between the produced electroweakino and the lightest SUSY particle (LSP) are targeted.

The use of fully-hadronic final states takes advantage of the large SM boson branching ratios, while the backgrounds are efficiently suppressed by reconstructing the W, Z and h bosons using the boosted boson tagging techniques. Using 139 fb^{-1}of proton-proton collision data at $\sqrt{s}$ = 13 TeV recorded by the ATLAS detector at LHC, this strategy allows for unprecedented sensitivity to the production of heavy electroweakinos.

No excess over the SM background predictions is observed, and 95% CL exclusion limits are set for signal models of various R-parity conserving scenarios. For wino pair production with direct decays into a bino and higgsino LSP, wino masses between 400 GeV and 1060 GeV are excluded when the LSP mass is below 400 GeV. For higgsino pair production with direct decays into a bino or wino LSP, higgsino masses between 450 GeV and 900 GeV are excluded when the LSP mass is below 240 GeV. The limits are also examined for varying wino (higgsino) branching ratio assumptions, by directly scanning over relevant branching ratios (for the bino LSP models) or over the MSSM parameters that dictate them (M_2, μ, and $\tan\beta$ for the wino/higgsino LSP models). The results are confirmed to be highly consistent for the variations.

The results are also interpreted in the context of simplified models of wino production with decays into a bino LSP, which are more conventionally explored in electroweakino searches at the LHC. For chargino pair production, with each decaying into a W-boson and an LSP, a chargino mass between 630 GeV and 760 GeV is excluded for an LSP mass below 80 GeV. For chargino-neutralino pair production involving decays to WZ (Wh) and two LSPs, a wino mass between 440 (400) GeV and 960 (1060) GeV is excluded for an LSP mass below 300 (420) GeV. These significantly extend the exclusion limits set by the previous searches at the LHC using different final states.

Finally, exclusion limits are set on higgsino production decaying into a massless gravitino LSP or a massless/massive axino LSP, motivated by the general gauge mediation model (GGM) or new physics models involving the axion, respectively. A higgsino mass between 450 (500) GeV and 940 (850) GeV is excluded for the gravitino LSP model with $\mathcal{B}(\widetilde{\chi}_1^0 \to Z\widetilde{G})$ = 100 (50)%; and between 450 (500) GeV and 940 (850) GeV is excluded for the axino LSP model with $\mathcal{B}(\widetilde{\chi}_1^0 \to Z\widetilde{G})$ = 100 (50)% when the axino LSP mass is below 300 (210) GeV.

References

[1] Y. Golfand and E. Likhtman,
Extension of the Algebra of Poincare Group Generators and Violation of P Invariance,
JETP Lett. **13** (1971) 323, [Pisma Zh. Eksp. Teor. Fiz. **13** (1971) 452] (cit. on p. 2).

[2] D. Volkov and V. Akulov, *Is the neutrino a goldstone particle?*, Phys. Lett. B **46** (1973) 109 (cit. on p. 2).

[3] J. Wess and B. Zumino, *Supergauge transformations in four dimensions*,
Nucl. Phys. B **70** (1974) 39 (cit. on p. 2).

[4] J. Wess and B. Zumino, *Supergauge invariant extension of quantum electrodynamics*, Nucl. Phys. B **78** (1974) 1 (cit. on p. 2).

[5] S. Ferrara and B. Zumino, *Supergauge invariant Yang-Mills theories*, Nucl. Phys. B **79** (1974) 413 (cit. on p. 2).

[6] A. Salam and J. Strathdee, *Super-symmetry and non-Abelian gauges*, Phys. Lett. B **51** (1974) 353 (cit. on p. 2).

[7] H. Goldberg, *Constraint on the Photino Mass from Cosmology*, Phys. Rev. Lett. **50** (1983) 1419 (cit. on p. 2).

[8] J. Ellis, J. Hagelin, D. V. Nanopoulos, K. A. Olive and M. Srednicki, *Supersymmetric relics from the big bang*, Nucl. Phys. B **238** (1984) 453 (cit. on p. 2).

[9] G. R. Farrar and P. Fayet, *Phenomenology of the production, decay, and detection of new hadronic states associated with supersymmetry*, Phys. Lett. B **76** (1978) 575 (cit. on p. 2).

[10] J. Hisano, S. Matsumot, M. Nagai, O. Saito and M. Senami, *Non-perturbative effect on thermal relic abundance of dark matter*, Physics Letters B **646** (2007) 34 , ISSN: 0370-2693, URL: http://www.sciencedirect.com/science/article/pii/S0370269307000913 (cit. on p. 2).

[11] T. Han, S. Mukhopadhyay and X. Wang, *Electroweak dark matter at future hadron colliders*, Phys. Rev. D **98** (3 2018) 035026, URL: https://link.aps.org/doi/10.1103/PhysRevD.98.035026 (cit. on p. 2).

[12] R. Barbieri and D. Pappadopulo, *S-particles at their naturalness limits*, JHEP **10** (2009) 061, arXiv: 0906.4546 [hep-ph] (cit. on p. 2).

[13] H. Baer, V. Barger and P. Huang, *Hidden SUSY at the LHC: the light higgsino-world scenario and the role of a lepton collider*, JHEP **11** (2011) 031, arXiv: 1107.5581 [hep-ph] (cit. on p. 2).

[14] M. Papucci, J. T. Ruderman and A. Weiler, *Natural SUSY endures*, JHEP **09** (2012) 035, arXiv: 1110.6926 [hep-ph] (cit. on p. 2).

[15] H. Baer, V. Barger, P. Huang, A. Mustafayev and X. Tata, *Radiative natural SUSY with a 125 GeV Higgs boson*, Phys. Rev. Lett. **109** (2012) 161802, arXiv: 1207.3343 [hep-ph] (cit. on p. 2).

[16] L. L. Everett, G. L. Kane, S. Rigolin and L.-T. Wang, *Implications of Muon $g-2$ for Supersymmetry and for Discovering Superpartners Directly*, Phys. Rev. Lett. **86** (16 2001) 3484, URL: https://link.aps.org/doi/10.1103/PhysRevLett.86.3484 (cit. on p. 2).

[17] M. Endo, K. Hamaguchi, S. Iwamoto and T. Kitahara, *Muon g- 2 vs LHC Run 2 in supersymmetric models*, Journal of High Energy Physics **2020** (2020) 1, URL: https://link.springer.com/article/10.1007/JHEP04(2020)165 (cit. on p. 2).

[18] ATLAS Collaboration, *Search for electroweak production of charginos and sleptons decaying into final states with two leptons and missing transverse momentum in $\sqrt{s} = 13$ TeV pp collisions using the ATLAS detector*, Eur. Phys. J. C **80** (2020) 123, arXiv: 1908.08215 [hep-ex] (cit. on pp. 2, 5, 7, 10, 33).

[19] ATLAS Collaboration, *Search for chargino-neutralino pair production in final states with three leptons and missing transverse momentum in $\sqrt{s} = 13$ TeV pp collisions with the ATLAS detector*, ATLAS-CONF-2020-015, 2020, URL: https://cds.cern.ch/record/2719521 (cit. on pp. 2, 5, 7, 32, 33).

[20] ATLAS Collaboration, *Search for chargino–neutralino production using recursive jigsaw reconstruction in final states with two or three charged leptons in proton–proton collisions at $\sqrt{s} = 13$ TeV with the ATLAS detector*, Phys. Rev. D **98** (2018) 092012, arXiv: 1806.02293 [hep-ex] (cit. on pp. 2, 5, 10, 32).

[21] ATLAS Collaboration, *Search for chargino–neutralino production with mass splittings near the electroweak scale in three-lepton final states in $\sqrt{s} = 13$ TeV pp collisions with the ATLAS detector*, Phys. Rev. D **101** (2020) 072001, arXiv: 1912.08479 [hep-ex] (cit. on pp. 2, 5, 10).

[22] ATLAS Collaboration, *Search for chargino and neutralino production in final states with a Higgs boson and missing transverse momentum at $\sqrt{s} = 13$ TeV with the ATLAS detector*, Phys. Rev. D **100** (2019) 012006, arXiv: 1812.09432 [hep-ex] (cit. on pp. 2, 3, 5, 10).

[23] ATLAS Collaboration, *Search for direct production of electroweakinos in final states with missing transverse momentum and a Higgs boson decaying into photons in pp collisions at $\sqrt{s} = 13$ TeV with the ATLAS detector*, JHEP **10** (2020) 005, arXiv: 2004.10894 [hep-ex] (cit. on pp. 2, 5, 10).

[24] ATLAS Collaboration, *Search for direct production of electroweakinos in final states with one lepton, missing transverse momentum and a Higgs boson decaying into two b-jets in pp collisions at $\sqrt{s} = 13$ TeV with the ATLAS detector*, Eur. Phys. J. C **80** (2020) 691, arXiv: 1909.09226 [hep-ex] (cit. on pp. 2, 5, 7, 10, 32, 33).

[25] ATLAS Collaboration, *Search for pair production of higgsinos in final states with at least three b-tagged jets in $\sqrt{s} = 13$ TeV pp collisions using the ATLAS detector*, Phys. Rev. D **98** (2018) 092002, arXiv: 1806.04030 [hep-ex] (cit. on pp. 2, 5, 32, 34).

[26] ATLAS Collaboration, *Search for supersymmetry in events with four or more charged leptons in 139 fb^{-1} of $\sqrt{s} = 13$ TeV pp collisions with the ATLAS detector*, (2021), arXiv: 2103.11684 [hep-ex] (cit. on pp. 2, 5, 32, 34).

[27] CMS Collaboration, *Searches for pair production of charginos and top squarks in final states with two oppositely charged leptons in proton–proton collisions at $\sqrt{s} = 13$ TeV*, JHEP **11** (2018) 079, arXiv: 1807.07799 [hep-ex] (cit. on pp. 2, 5, 10).

[28] CMS Collaboration, *Search for new phenomena in final states with two opposite-charge, same-flavor leptons, jets, and missing transverse momentum in pp collisions at $\sqrt{s} = 13$ TeV*, JHEP **03** (2018) 076, arXiv: 1709.08908 [hep-ex] (cit. on pp. 2, 5, 10).

[29] CMS Collaboration, *Combined search for electroweak production of charginos and neutralinos in proton–proton collisions at $\sqrt{s} = 13$ TeV*, JHEP **03** (2018) 160, arXiv: 1801.03957 [hep-ex] (cit. on pp. 2, 5, 10).

[30] CMS Collaboration, *Search for electroweak production of charginos and neutralinos in multilepton final states in proton–proton collisions at $\sqrt{s} = 13$ TeV*, JHEP **03** (2018) 166, arXiv: 1709.05406 [hep-ex] (cit. on pp. 2, 5, 10).

[31] CMS Collaboration, *Search for electroweak production of charginos and neutralinos in WH events in proton–proton collisions at* $\sqrt{s} = 13$ *TeV*, JHEP **11** (2017) 029, arXiv: 1706.09933 [hep-ex] (cit. on pp. 2, 5, 10).

[32] CMS Collaboration, *Search for supersymmetry with Higgs boson to diphoton decays using the razor variables at* $\sqrt{s} = 13$ *TeV*, Phys. Lett. B **779** (2018) 166, arXiv: 1709.00384 [hep-ex] (cit. on pp. 2, 5, 10).

[33] CMS Collaboration, *Search for Higgsino pair production in pp collisions at* $\sqrt{s} = 13$ *TeV in final states with large missing transverse momentum and two Higgs bosons decaying via* $H \to b\bar{b}$, Phys. Rev. D **97** (2018) 032007, arXiv: 1709.04896 [hep-ex] (cit. on p. 2).

[34] ATLAS Collaboration, *Performance of top-quark and W-boson tagging with ATLAS in Run 2 of the LHC*, Eur. Phys. J. C **79** (2019) 375, arXiv: 1808.07858 [hep-ex] (cit. on pp. 3, 10, 11).

[35] ATLAS Collaboration, *Identification of boosted Higgs bosons decaying into b-quark pairs with the ATLAS detector at* 13 *TeV*, Eur. Phys. J. C **79** (2019) 836, arXiv: 1906.11005 [hep-ex] (cit. on p. 3).

[36] CMS Collaboration, *Identification techniques for highly boosted W bosons that decay into hadrons*, JHEP **12** (2014) 017, arXiv: 1410.4227 [hep-ex] (cit. on p. 3).

[37] CMS Collaboration, *Identification of heavy-flavour jets with the CMS detector in pp collisions at* 13 *TeV*, JINST **13** (2018) P05011, arXiv: 1712.07158 [hep-ex] (cit. on p. 3).

[38] G. Giudice and A. Romanino, *Split supersymmetry*, Nucl. Phys. B **699** (2004) 65, arXiv: hep-ph/0406088 (cit. on p. 3).

[39] N. Arkani-Hamed and S. Dimopoulos, *Supersymmetric unification without low energy supersymmetry and signatures for fine-tuning at the LHC*, JHEP **06** (2005) 073, arXiv: hep-th/0405159 (cit. on p. 3).

[40] T. Han, S. Padhi and S. Su, *Electroweakinos in the light of the Higgs boson*, Phys. Rev. D **88** (11 2013) 115010, URL: https://link.aps.org/doi/10.1103/PhysRevD.88.115010 (cit. on p. 4).

[41] B. C. Allanach, *SOFTSUSY: a program for calculating supersymmetric spectra*, Comput. Phys. Commun. **143** (2002) 305, arXiv: hep-ph/0104145 [hep-ph] (cit. on p. 4).

[42] B. C. Allanach and T. Cridge, *The Calculation of Sparticle and Higgs Decays in the Minimal and Next-to-Minimal Supersymmetric Standard Models: SOFTSUSY4.0*, (2017), arXiv: 1703.09717 [hep-ph] (cit. on p. 4).

[43] P. Meade, N. Seiberg and D. Shih, *General Gauge Mediation*, Prog. Theor. Phys. Suppl. **177** (2009) 143, arXiv: 0801.3278 [hep-ph] (cit. on p. 5).

[44] C. Cheung, A. L. Fitzpatrick and D. Shih, *(Extra)ordinary gauge mediation*, JHEP **07** (2008) 054, arXiv: 0710.3585 [hep-ph] (cit. on p. 5).

[45] M. Dine and W. Fischler, *A phenomenological model of particle physics based on supersymmetry*, Phys. Lett. B **110** (1982) 227 (cit. on p. 5).

[46] L. Alvarez-Gaumé, M. Claudson and M. B. Wise, *Low-energy supersymmetry*, Nucl. Phys. B **207** (1982) 96 (cit. on p. 5).

[47] C. R. Nappi and B. A. Ovrut, *Supersymmetric extension of the SU(3) x SU(2) x U(1) model*, Phys. Lett. B **113** (1982) 175 (cit. on p. 5).

[48] R. D. Peccei and H. R. Quinn, *CP Conservation in the Presence of Instantons*, Phys. Rev. Lett **38** (1977) 328, URL: https://journals.aps.org/prl/abstract/10.1103/PhysRevLett.38.1440 (cit. on p. 5).

[49] S. Weinberg, *A new light boson?*, Physical Review Letters **40** (1978) 223, URL: https://journals.aps.org/prl/abstract/10.1103/PhysRevLett.40.223 (cit. on p. 5).

[50] F. Wilczek, *Problem of Strong P and T Invariance in the Presence of Instantons*, Physical Review Letters **40** (1978) 279, URL: https://journals.aps.org/prl/abstract/10.1103/PhysRevLett.40.279 (cit. on p. 5).

[51] G. Barenboim, E. J. Chun, S. Jung and W. I. Park, *Implications of an axino LSP for naturalness*, Phys. Rev. D **90** (3 2014) 035020, URL: https://link.aps.org/doi/10.1103/PhysRevD.90.035020 (cit. on p. 6).

[52] L. Covi and J. E. Kim, *Axinos as dark matter particles*, New Journal of Physics **11** (2009) 105003, URL: https://iopscience.iop.org/article/10.1088/1367-2630/11/10/105003 (cit. on p. 6).

[53] K. J. Bae, E. J. Chun and S. H. Im, *Cosmology of the DFSZ axino*, Journal of Cosmology and Astroparticle Physics **2012** (2012) 013, URL: https://iopscience.iop.org/article/10.1088/1475-7516/2012/03/013 (cit. on p. 6).

[54] ATLAS Collaboration, *Search for electroweak production of supersymmetric particles in final states with two or three leptons at $\sqrt{s}$ = 13 TeV with the ATLAS detector*, Eur. Phys. J. C **78** (2018) 995, arXiv: 1803.02762 [hep-ex] (cit. on p. 7).

[55] ATLAS Collaboration, *The ATLAS Experiment at the CERN Large Hadron Collider*, JINST **3** (2008) S08003 (cit. on p. 6).

[56] B. Abbott et al., *Production and integration of the ATLAS Insertable B-Layer*, JINST **13** (2018) T05008, arXiv: 1803.00844 [physics.ins-det] (cit. on p. 6).

[57] ATLAS Collaboration, *Performance of the ATLAS trigger system in 2015*, Eur. Phys. J. C **77** (2017) 317, arXiv: 1611.09661 [hep-ex] (cit. on p. 7).

[58] ATLAS Collaboration, *ATLAS data quality operations and performance for 2015–2018 data-taking*, JINST **15** (2020) P04003, arXiv: 1911.04632 [physics.ins-det] (cit. on p. 7).

[59] ATLAS Collaboration, *Performance of the missing transverse momentum triggers for the ATLAS detector during Run-2 data taking*, JHEP **08** (2020) 080, arXiv: 2005.09554 [hep-ex] (cit. on p. 7).

[60] ATLAS Collaboration, *Performance of electron and photon triggers in ATLAS during LHC Run 2*, Eur. Phys. J. C **80** (2020) 47, arXiv: 1909.00761 [hep-ex] (cit. on pp. 8, 20).

[61] ATLAS Collaboration, *Performance of the ATLAS muon triggers in Run 2*, JINST **15** (2020) P09015, arXiv: 2004.13447 [hep-ex] (cit. on p. 8).

[62] ATLAS Collaboration, *The ATLAS Simulation Infrastructure*, Eur. Phys. J. C **70** (2010) 823, arXiv: 1005.4568 [physics.ins-det] (cit. on p. 8).

[63] GEANT4 Collaboration, S. Agostinelli et al., *GEANT4 – a simulation toolkit*, Nucl. Instrum. Meth. A **506** (2003) 250 (cit. on p. 8).

[64] T. Sjöstrand, S. Mrenna and P. Skands, *A brief introduction to PYTHIA 8.1*, Comput. Phys. Commun. **178** (2008) 852, arXiv: 0710.3820 [hep-ph] (cit. on p. 8).

[65] ATLAS Collaboration, *The Pythia 8 A3 tune description of ATLAS minimum bias and inelastic measurements incorporating the Donnachie–Landshoff diffractive model*, ATL-PHYS-PUB-2016-017, 2016, URL: https://cds.cern.ch/record/2206965 (cit. on p. 8).

[66] R. D. Ball et al., *Parton distributions with LHC data*, Nucl. Phys. B **867** (2013) 244, arXiv: 1207.1303 [hep-ph] (cit. on p. 8).

[67] E. Bothmann et al., *Event Generation with Sherpa 2.2*, (2019), arXiv: 1905.09127 [hep-ph] (cit. on p. 8).

[68] T. Gleisberg and S. Höche, *Comix, a new matrix element generator*, JHEP **12** (2008) 039, arXiv: 0808.3674 [hep-ph] (cit. on p. 8).

[69] F. Cascioli, P. Maierhofer and S. Pozzorini, *Scattering Amplitudes with Open Loops*, Phys. Rev. Lett. **108** (2012) 111601, arXiv: 1111.5206 [hep-ph] (cit. on p. 8).

[70] A. Denner, S. Dittmaier and L. Hofer, *Collier: A fortran-based complex one-loop library in extended regularizations*, Comput. Phys. Commun. **212** (2017) 220, arXiv: 1604.06792 [hep-ph] (cit. on p. 8).

[71] S. Höche, F. Krauss, M. Schönherr and F. Siegert, *A critical appraisal of NLO+PS matching methods*, JHEP **09** (2012) 049, arXiv: 1111.1220 [hep-ph] (cit. on p. 8).

[72] S. Catani, F. Krauss, R. Kuhn and B. R. Webber, *QCD Matrix Elements + Parton Showers*, JHEP **11** (2001) 063, arXiv: hep-ph/0109231 (cit. on p. 8).

[73] S. Höche, F. Krauss, S. Schumann and F. Siegert, *QCD matrix elements and truncated showers*, JHEP **05** (2009) 053, arXiv: 0903.1219 [hep-ph] (cit. on p. 8).

[74] S. Höche, F. Krauss, M. Schönherr and F. Siegert, *QCD matrix elements + parton showers. The NLO case*, JHEP **04** (2013) 027, arXiv: 1207.5030 [hep-ph] (cit. on p. 8).

[75] NNPDF Collaboration, R.D. Ball et al., *Parton distributions for the LHC Run II*, JHEP **04** (2015) 040, arXiv: 1410.8849 [hep-ph] (cit. on p. 8).

[76] S. Frixione, *Isolated photons in perturbative QCD*, Phys. Lett. B **429** (1998) 369, arXiv: hep-ph/9801442 (cit. on p. 8).

[77] S. Frixione, P. Nason and G. Ridolfi, *A positive-weight next-to-leading-order Monte Carlo for heavy flavour hadroproduction*, JHEP **09** (2007) 126, arXiv: 0707.3088 [hep-ph] (cit. on p. 8).

[78] P. Nason, *A new method for combining NLO QCD with shower Monte Carlo algorithms*, JHEP **11** (2004) 040, arXiv: hep-ph/0409146 (cit. on p. 8).

[79] S. Frixione, P. Nason and C. Oleari,
Matching NLO QCD computations with Parton Shower simulations: the POWHEG method,
JHEP **11** (2007) 070, arXiv: 0709.2092 [hep-ph] (cit. on p. 8).

[80] S. Alioli, P. Nason, C. Oleari and E. Re, *A general framework for implementing NLO calculations in shower Monte Carlo programs: the POWHEG BOX*, JHEP **06** (2010) 043,
arXiv: 1002.2581 [hep-ph] (cit. on p. 8).

[81] ATLAS Collaboration, *Studies on top-quark Monte Carlo modelling for Top2016*,
ATL-PHYS-PUB-2016-020, 2016, URL: https://cds.cern.ch/record/2216168
(cit. on p. 8).

[82] ATLAS Collaboration, *ATLAS Pythia 8 tunes to 7 TeV data*, ATL-PHYS-PUB-2014-021, 2014,
URL: https://cds.cern.ch/record/1966419 (cit. on pp. 8, 10).

[83] D. J. Lange, *The EvtGen particle decay simulation package*,
Nucl. Instrum. Meth. A **462** (2001) 152 (cit. on p. 8).

[84] S. Frixione, E. Laenen, P. Motylinski, B. R. Webber and C. D. White,
Single-top hadroproduction in association with a W boson, JHEP **07** (2008) 029,
arXiv: 0805.3067 [hep-ph] (cit. on p. 8).

[85] J. Alwall et al., *The automated computation of tree-level and next-to-leading order differential cross sections, and their matching to parton shower simulations*, JHEP **07** (2014) 079,
arXiv: 1405.0301 [hep-ph] (cit. on p. 8).

[86] M. Beneke, P. Falgari, S. Klein and C. Schwinn,
Hadronic top-quark pair production with NNLL threshold resummation,
Nucl. Phys. B **855** (2012) 695, arXiv: 1109.1536 [hep-ph] (cit. on p. 9).

[87] M. Cacciari, M. Czakon, M. Mangano, A. Mitov and P. Nason, *Top-pair production at hadron colliders with next-to-next-to-leading logarithmic soft-gluon resummation*,
Phys. Lett. B **710** (2012) 612, arXiv: 1111.5869 [hep-ph] (cit. on p. 9).

[88] P. Bärnreuther, M. Czakon and A. Mitov, *Percent-Level-Precision Physics at the Tevatron: Next-to-Next-to-Leading Order QCD Corrections to $q\bar{q} \to t\bar{t} + X$*,
Phys. Rev. Lett. **109** (2012) 132001, arXiv: 1204.5201 [hep-ph] (cit. on p. 9).

[89] M. Czakon and A. Mitov,
NNLO corrections to top-pair production at hadron colliders: the all-fermionic scattering channels,
JHEP **12** (2012) 054, arXiv: 1207.0236 [hep-ph] (cit. on p. 9).

[90] M. Czakon and A. Mitov,
NNLO corrections to top pair production at hadron colliders: the quark-gluon reaction,
JHEP **01** (2013) 080, arXiv: 1210.6832 [hep-ph] (cit. on p. 9).

[91] M. Czakon, P. Fiedler and A. Mitov,
Total Top-Quark Pair-Production Cross Section at Hadron Colliders Through $O(\alpha_S^4)$,
Phys. Rev. Lett. **110** (2013) 252004, arXiv: 1303.6254 [hep-ph] (cit. on p. 9).

[92] M. Czakon and A. Mitov,
Top++: A program for the calculation of the top-pair cross-section at hadron colliders,
Comput. Phys. Commun. **185** (2014) 2930, arXiv: 1112.5675 [hep-ph] (cit. on p. 9).

[93] P. Kant et al., *HatHor for single top-quark production: Updated predictions and uncertainty estimates for single top-quark production in hadronic collisions*,
Comput. Phys. Commun. **191** (2015) 74, arXiv: 1406.4403 [hep-ph] (cit. on p. 9).

[94] M. Aliev et al., *HATHOR – HAdronic Top and Heavy quarks crOss section calculatoR*, Comput. Phys. Commun. **182** (2011) 1034, arXiv: 1007.1327 [hep-ph] (cit. on p. 9).

[95] N. Kidonakis, *Next-to-next-to-leading-order collinear and soft gluon corrections for t-channel single top quark production*, Phys. Rev. D **83** (2011) 091503, arXiv: 1103.2792 [hep-ph] (cit. on p. 9).

[96] N. Kidonakis, *Two-loop soft anomalous dimensions for single top quark associated production with a W- or H-*, Phys. Rev. **D82** (2010) 054018, arXiv: 1005.4451 [hep-ph] (cit. on p. 9).

[97] A. Lazopoulos, T. McElmurry, K. Melnikov and F. Petriello, *Next-to-leading order QCD corrections to $t\bar{t}Z$ production at the LHC*, Phys. Lett. B **666** (2008) 62, arXiv: 0804.2220 [hep-ph] (cit. on p. 9).

[98] J. M. Campbell and R. Ellis, *$t\bar{t}W^{+-}$ production and decay at NLO*, JHEP **07** (2012) 052, arXiv: 1204.5678 [hep-ph] (cit. on p. 9).

[99] J. M. Campbell, R. K. Ellis and C. Williams, *Vector boson pair production at the LHC*, JHEP **07** (2011) 018, arXiv: 1105.0020 [hep-ph] (cit. on p. 9).

[100] C. Anastasiou, L. J. Dixon, K. Melnikov and F. Petriello, *High precision QCD at hadron colliders: Electroweak gauge boson rapidity distributions at NNLO*, Phys. Rev. D **69** (2004) 094008, arXiv: hep-ph/0312266 (cit. on p. 9).

[101] T. Sjöstrand et al., *An introduction to PYTHIA 8.2*, Comput. Phys. Commun. **191** (2015) 159, arXiv: 1410.3012 [hep-ph] (cit. on p. 10).

[102] P. Artoisenet, R. Frederix, O. Mattelaer and R. Rietkerk, *Automatic spin-entangled decays of heavy resonances in Monte Carlo simulations*, JHEP **03** (2013) 015, arXiv: 1212.3460 [hep-ph] (cit. on p. 10).

[103] S. Frixione, E. Laenen, P. Motylinski and B. R. Webber, *Angular correlations of lepton pairs from vector boson and top quark decays in Monte Carlo simulations*, JHEP **04** (2007) 081, arXiv: hep-ph/0702198 (cit. on p. 10).

[104] J. Butterworth et al., *PDF4LHC recommendations for LHC Run II*, J. Phys. G **43** (2016) 023001, arXiv: 1510.03865 [hep-ph] (cit. on p. 10).

[105] ATLAS Collaboration, *Topological cell clustering in the ATLAS calorimeters and its performance in LHC Run 1*, Eur. Phys. J. C **77** (2017) 490, arXiv: 1603.02934 [hep-ex] (cit. on p. 10).

[106] M. Cacciari, G. P. Salam and G. Soyez, *The anti-k_t jet clustering algorithm*, JHEP **04** (2008) 063, arXiv: 0802.1189 [hep-ph] (cit. on p. 10).

[107] M. Cacciari, G. P. Salam and G. Soyez, *FastJet user manual*, Eur. Phys. J. C **72** (2012) 1896, arXiv: 1111.6097 [hep-ph] (cit. on p. 10).

[108] D. Krohn, J. Thaler and L.-T. Wang, *Jet trimming*, JHEP **02** (2010) 084, arXiv: 0912.1342 [hep-ph] (cit. on p. 10).

[109] S. D. Ellis and D. E. Soper, *Successive combination jet algorithm for hadron collisions*, Phys. Rev. D **48** (1993) 3160, arXiv: hep-ph/9305266 [hep-ph] (cit. on p. 10).

[110] ATLAS Collaboration, *Jet mass reconstruction with the ATLAS Detector in early Run 2 data*, ATLAS-CONF-2016-035, 2016, URL: https://cds.cern.ch/record/2200211 (cit. on p. 10).

[111] ATLAS Collaboration, *In situ calibration of large-radius jet energy and mass in* 13 *TeV proton–proton collisions with the ATLAS detector*, Eur. Phys. J. C **79** (2019) 135, arXiv: 1807.09477 [hep-ex] (cit. on pp. 10, 20).

[112] ATLAS Collaboration, *Variable Radius, Exclusive-k_T, and Center-of-Mass Subjet Reconstruction for Higgs($\to b\bar{b}$) Tagging in ATLAS*, ATL-PHYS-PUB-2017-010, 2017, URL: https://cds.cern.ch/record/2268678 (cit. on p. 11).

[113] ATLAS Collaboration, *ATLAS b-jet identification performance and efficiency measurement with $t\bar{t}$ events in pp collisions at $\sqrt{s}$ = 13 TeV*, Eur. Phys. J. C **79** (2019) 970, arXiv: 1907.05120 [hep-ex] (cit. on p. 11).

[114] ATLAS Collaboration, *Calibration of the ATLAS b-tagging algorithm in $t\bar{t}$ semileptonic events*, ATLAS-CONF-2018-045, 2018, URL: https://cds.cern.ch/record/2638455 (cit. on p. 11).

[115] ATLAS Collaboration, *Calibration of light-flavour b-jet mistagging rates using ATLAS proton–proton collision data at $\sqrt{s}$ = 13 TeV*, ATLAS-CONF-2018-006, 2018, URL: https://cds.cern.ch/record/2314418 (cit. on p. 11).

[116] ATLAS Collaboration, *Boosted hadronic vector boson and top quark tagging with ATLAS using Run 2 data*, ATL-PHYS-PUB-2020-017, 2020, URL: https://cds.cern.ch/record/2724149 (cit. on pp. 11, 19, 20).

[117] A. J. Larkoski, G. P. Salam and J. Thaler, *Energy Correlation Functions for Jet Substructure*, JHEP **06** (2013) 108, arXiv: 1305.0007 [hep-ph] (cit. on p. 11).

[118] A. J. Larkoski, I. Moult and D. Neill, *Power Counting to Better Jet Observables*, JHEP **12** (2014) 009, arXiv: 1409.6298 [hep-ph] (cit. on p. 11).

[119] ATLAS Collaboration, *Electron and photon performance measurements with the ATLAS detector using the 2015–2017 LHC proton–proton collision data*, JINST **14** (2019) P12006, arXiv: 1908.00005 [hep-ex] (cit. on pp. 11–13, 20).

[120] ATLAS Collaboration, *Muon reconstruction and identification efficiency in ATLAS using the full Run 2 pp collision data set at $\sqrt{s}$ = 13 TeV*, (2020), arXiv: 2012.00578 [hep-ex] (cit. on pp. 11, 13).

[121] ATLAS Collaboration, *Jet reconstruction and performance using particle flow with the ATLAS Detector*, Eur. Phys. J. C **77** (2017) 466, arXiv: 1703.10485 [hep-ex] (cit. on p. 11).

[122] ATLAS Collaboration, *Performance of pile-up mitigation techniques for jets in pp collisions at $\sqrt{s}$ = 8 TeV using the ATLAS detector*, Eur. Phys. J. C **76** (2016) 581, arXiv: 1510.03823 [hep-ex] (cit. on pp. 12, 13).

[123] ATLAS Collaboration, *Jet energy scale measurements and their systematic uncertainties in proton–proton collisions at $\sqrt{s}$ = 13 TeV with the ATLAS detector*, Phys. Rev. D **96** (2017) 072002, arXiv: 1703.09665 [hep-ex] (cit. on pp. 12, 20).

[124] ATLAS Collaboration, *Muon reconstruction and identification efficiency in ATLAS using the full Run 2 pp collision data set at $\sqrt{s}$ = 13 TeV*, ATLAS-CONF-2020-030, 2020, URL: https://cds.cern.ch/record/2725736 (cit. on p. 12).

[125] ATLAS Collaboration, *Performance of missing transverse momentum reconstruction with the ATLAS detector using proton–proton collisions at $\sqrt{s}$ = 13 TeV*, Eur. Phys. J. C **78** (2018) 903, arXiv: 1802.08168 [hep-ex] (cit. on pp. 13, 20).

[126] ATLAS Collaboration, *Tagging and suppression of pileup jets with the ATLAS detector*, ATLAS-CONF-2014-018, 2014, URL: https://cds.cern.ch/record/1700870 (cit. on p. 13).

[127] ATLAS Collaboration, *Vertex Reconstruction Performance of the ATLAS Detector at* $\sqrt{s} = 13$ *TeV*, ATL-PHYS-PUB-2015-026, 2015, URL: https://cds.cern.ch/record/2037717 (cit. on p. 13).

[128] ATLAS Collaboration, *Non-collision backgrounds as measured by the ATLAS detector during the 2010 proton–proton run*, ATLAS-CONF-2011-137, 2011, URL: https://cds.cern.ch/record/1383840 (cit. on p. 13).

[129] ATLAS Collaboration, *Selection of jets produced in* 13 *TeV proton–proton collisions with the ATLAS detector*, ATLAS-CONF-2015-029, 2015, URL: https://cds.cern.ch/record/2037702 (cit. on p. 13).

[130] C. G. Lester and D. J. Summers, *Measuring masses of semiinvisibly decaying particles pair produced at hadron colliders*, Phys. Lett. B **463** (1999) 99, arXiv: hep-ph/9906349 [hep-ph] (cit. on p. 15).

[131] A. Barr, C. Lester and P. Stephens, m_{T2}*: The Truth behind the glamour*, J. Phys. G **29** (2003) 2343, arXiv: hep-ph/0304226 [hep-ph] (cit. on p. 15).

[132] ATLAS Collaboration, *Search for squarks and gluinos in final states with jets and missing transverse momentum using* $139\,fb^{-1}$ *of* $\sqrt{s} = 13$ *TeV* pp *collision data with the ATLAS detector*, JHEP **02** (2021) 143, arXiv: 2010.14293 [hep-ex] (cit. on p. 16).

[133] ATLAS Collaboration, *Evidence for the production of three massive vector bosons with the ATLAS detector*, Phys. Lett. B **798** (2019) 134913, arXiv: 1903.10415 [hep-ex] (cit. on p. 16).

[134] CMS Collaboration, *Observation of the production of three massive gauge bosons at* $\sqrt{s} = 13$ *TeV*, Phys. Rev. Lett. **125** (2020) 151802, arXiv: 2006.11191 [hep-ex] (cit. on p. 16).

[135] ATLAS Collaboration, *Measurement of the WW cross section in* $\sqrt{s} = 7$ *TeV* pp *collisions with the ATLAS detector and limits on anomalous gauge couplings*, Phys. Lett. B **712** (2012) 289, arXiv: 1203.6232 [hep-ex] (cit. on p. 18).

[136] ATLAS Collaboration, *Measurement of the inclusive isolated prompt photon cross section in* pp *collisions at* $\sqrt{s} = 7$ *TeV with the ATLAS detector*, Phys. Rev. D **83** (2011) 052005, arXiv: 1012.4389 [hep-ex] (cit. on p. 18).

[137] ATLAS Collaboration, *Muon reconstruction and identification efficiency in ATLAS using the full Run 2* pp *collision data set at* $\sqrt{s} = 13$ *TeV*, (2020), Submitted to Eur. Phys. J. C., arXiv: 2012.00578 [hep-ex], URL: https://cds.cern.ch/record/2746368 (cit. on p. 20).

[138] ATLAS Collaboration, *Muon reconstruction performance of the ATLAS detector in proton–proton collision data at* $\sqrt{s} = 13$ *TeV*, Eur. Phys. J. C **76** (2016) 292, arXiv: 1603.05598 [hep-ex] (cit. on p. 20).

[139] G. Avoni et al., *The new LUCID-2 detector for luminosity measurement and monitoring in ATLAS*, JINST **13** (2018) P07017 (cit. on p. 21).

[140] ATLAS Collaboration, *Measurement of the Inelastic Proton–Proton Cross Section at* $\sqrt{s} = 13$ *TeV with the ATLAS Detector at the LHC*, Phys. Rev. Lett. **117** (2016) 182002, arXiv: 1606.02625 [hep-ex] (cit. on p. 21).

[141] ATLAS Collaboration, *Monte Carlo Generators for the Production of a W or Z/γ^* Boson in Association with Jets at ATLAS in Run 2*, ATL-PHYS-PUB-2016-003, 2016, URL: https://cds.cern.ch/record/2120133 (cit. on p. 21).

[142] J. Bellm et al., *Herwig 7.0/Herwig++ 3.0 release note*, Eur. Phys. J. C **76** (2016) 196, arXiv: 1512.01178 [hep-ph] (cit. on p. 22).

[143] ATLAS Collaboration, *Improvements in $t\bar{t}$ modelling using NLO+PS Monte Carlo generators for Run 2*, ATL-PHYS-PUB-2018-009, 2018, URL: https://cds.cern.ch/record/2630327 (cit. on p. 22).

[144] G. Cowan, K. Cranmer, E. Gross and O. Vitells, *Asymptotic formulae for likelihood-based tests of new physics*, Eur. Phys. J. C **71** (2011) 1554, arXiv: 1007.1727 [physics.data-an] (cit. on p. 23).

[145] G. Cowan, K. Cranmer, E. Gross and O. Vitells, Eur. Phys. J. C **73** (2013) 2501 (cit. on p. 23).

[146] M. Baak et al., *HistFitter software framework for statistical data analysis*, Eur. Phys. J. C **75** (2015) 153, arXiv: 1410.1280 [hep-ex] (cit. on p. 23).

[147] A. L. Read, *Presentation of search results: the CL_S technique*, J. Phys. G **28** (2002) 2693 (cit. on p. 24).